LUND UNIVERSITY

Master of Science
Thesis
VT2023

Characterization of Carotid Atherosclerotic Stenosis on Photon-Counting Computed Tomography

My Celander

Supervisors

Marie-Louise Aurumskjöld, Veronica Fransson, and Kristina Ydström

Medical Radiation Physics, Lund
Faculty of Science
Lund University
www.msf.lu.se

Populärvetenskaplig sammanfattning

Stroke är när patienten får en blödning eller blodpropp i hjärnan som kan orsaka tal och rörelsebortfall, och i värsta fall en plötslig död. Åderförkalkning i halskärlen orsakar kring $10\% - 20\%$ av alla stroke-fall. Den nuvarande metoden som används för att bedöma åderförkalkningen är att mäta förträngningen av blodkärlet i skiktröntgenbilder (3D-röntgenbilder). Förträngning av blodkärlet säger ingenting om hur stor risken är att åderförkalkningen orsakar stroke. Det är snarare innehållet av åderförkalkningen som avgör denna risk. En åderförkalkning som till exempel, innehåller blödningar och består av en stor andel fett har större risk att orsaka stroke.

Dagens skiktröntgenbilder har begränsad upplösning vilket ger begränsad information om innehållet i åderförkalkningen. Om åderförkalkningen är rik på kalk kan detta överskugga resten av innehållet vilket kan göra att man missbedömer mätningarna av förträngningar. Med en fotonräknade skiktröntgen finns det potential att se mer innehåll i åderförkalkningen då den har bättre upplösning, kan minska bruset i bilderna och skapa bilder med annorlunda och förbättrad kontrast jämfört tidigare skiktröntgensystem. Målet med denna studie är att undersöka om det går att skilja på olika materialen som åderförkalkningen innehåller då man använder fotonräknade skiktröntgen bilder jämfört med vanliga skiktröntgen bilder med kemiskt infärgad åderförkalkning som referens.

Patienten som valdes ut till detta arbete hade symtom på åderförkalkning i halskärlen samt var kandidat för att operera bort åderförkalkningen. Patienten undersöktes i fotonräknande skiktröntgen enligt befintliga kliniska rutiner. Åderförkalkningen opererades därefter ut ur patienten, och för att kunna analysera innehållet blev det först nedfryst, sedan torkat och till sist inbäddat i paraffin. Nya bilder togs i fotonräknande skiktröntgen av den inbäddade åderförkalkningen. Innehållet i åderförkalkningen färgades sedan in med kemiska medel så att olika material får olika färg.

Bilderna från fotonräknande skiktröntgen, före och efter operation, jämfördes mot de kemiskt infärgade bilderna för att kunna använda de infärgade bilder som en karta, som berättar var i skiktröntgenbilderna som olika material finns. Utöver en ren visuell bedömning av bilderna mätte man bildvärdena på dessa material för att ta reda på om de går att särskilja från varandra. Samma mätningar utfördes upprepade gånger men med olika kontrastnivåer som den fotonräknande skiktröntgen kunde skapa.

Studiens resultat visade på att det inte går att se någon skillnad mellan material i åderförkalkningen för patientens skiktröntgenbilder medan det var möjligt att urskilja olika material för bilderna tagna på åderförkalkningen när den opererats ut ur patienten. En oväntad upptäckt var att det var möjligt att utföra en jämförelse mellan infärgad åderförkalkning och patientens skiktröntgenbilder, även om utseendet av den infärgade åderförkalkningen är mest lik bilderna av den utoperarade åderförkalkningen. Det är viktigt att nämna att bilderna tagna med den fotonräknande skiktröntgen var mycket bättre om man jämför med vanliga skiktröntgenbilder, eftersom man kunde se åderförkalkningen tydligare. Denna upptäckt är värdefull då det innebär att användning av fotonräknande skiktröntgenbilder kan öka säkerheten i bedömningen av åderförkalkningen, och leda till att fler patienter får en bättre behandling.

Abstract

Introduction and aim

Atherosclerotic stenosis located at the carotid bifurcation accounts for $10\% - 20\%$ of all Transient Ischemic Attacks (TIA) and ischemic strokes, which occurs when Atherosclerotic stenosis, or so-called plaque, ruptures. The current method to evaluate carotid atherosclerotic stenosis is to measure the degree of stenosis. Strong markers for plaque rupture lie in the plaque content, and not in the degree of stenosis. Conventional Computed Tomography (CT) does not have the soft tissue resolution to differentiate the material content of the plaque. Photon Counting Computed Tomography (PCCT) has the potential to perform better plaque imaging due to its improved noise reduction, energy resolution, and image reconstruction algorithm. The aim of this project is to investigate if the PCCT images can differentiate materials in carotid atherosclerotic stenosis (*ex vivo* and *in vivo*), by using histopathological images as a reference.

Materials and method

A photon-counting CT, Siemens Naeotom Alpha, was used for scanning in this project. One patient with symptoms of atherosclerotic stenosis was examined on the PCCT using the clinical protocol. Carotid endarterectomy was performed and the removed plaque was encased in paraffin before being imaged once again at the PCCT. Histopathology analysis stained the interesting materials in *ex vivo*. The result of the staining was used to define the Region Of Interest (ROI) in the *ex vivo* and *in vivo* PCCT images. One-way ANOVA was performed to determine if statistically significant differences in the Hounsfeild Unit (HU) of each material in Virtual Monoenergetic Images (VMI) (40190 keV in steps of ten) existed, the CI = 95.0%. If a statistical significance was found two-sided t-test found the exact materials that were significantly separated. Bonferroni correction was performed to reduce the risk of type 1 errors, resulting in the CI = 99.2%. A visual comparison of the *in vivo* images was also performed between conventional CT and PCCT systems.

Result

The one-way ANOVA test yielded statistical significance for all monoenergetic energy levels in the *ex vivo* measurements. The consecutive t-tests, however, showed no statistical significance for any energy or material after correcting for multiple tests. The one-way ANOVA performed on the *in vivo* measurement did not show any statistical significance for any energy. The appearance of *in vivo* images from the conventional CT and the PCCT system was very different. The calcium blooming was less prominent and structures that were invisible on the conventional CT system could be distinguished on the PCCT system.

Conclusion

The materials could not be statistically significantly differentiated in the *in vivo* PCCT images. *ex vivo* PCCT provided a larger difference in HU for different materials, but not significantly so. However, due to limited measurements, no certain conclusions could be drawn. The visual difference between *in vivo* images acquired by a PCCT and a conventional CT was considerable which could be valuable in the clinic due to the importance of good image quality when evaluating carotid atherosclerotic stenosis.

Abbreviations

BP	Back Projection
CC	Common Carotid
CCA	Common Carotid artery
CI	Confidence Internal
CNR	Contrast to Noise Ratio
CT	Computed Tomography
CTA	Computed Tomography Angiography
DECT	Dual-Energy Computed Tomography
ECA	External Carotid artery
ECST	European Carotid Surgery Trial
EID	Energy Integrating Detector
FBP	Filtered Back Projection
HU	Hounsfield Unit
ICA	Internal Carotid artery
IPH	Intra Plaque Hemorrhage
IR	Iterative Reconstruction
LRNC	Lipid-Rich Necrotic Core
MBIR	Model Based Iterative Reconstruction
MRA	Magnetic Resonance Angiography
NASCET	North American Symptomatic Carotid Endarterectomy Trial
PCD	Photon Counting Detector
PCCT	Photon Counting Computed Tomography
QIR	Quantum Iterative Reconstruction
ROI	Region Of Interest
SNR	Signal to Noise Ratio
TIA	Transient Ischaemic Attacks
UHR	Ultra-High Resolution
VMI	Virtual Monoenergetic Image

Contents

1 Introduction

Atherosclerotic stenosis located at the carotid bifurcation accounts for $10\% - 20\%$ of all Transient Ischaemic Attacks (TIA) and ischaemic strokes [1]. A TIA is a reversible brain ischemia caused by occlusion of blood vessels. The occlusion could be due to the stenosis (plaque) itself or a thrombus (stationary or floating blood clot) originating from plaque rupture [2–4].

The modalities used for evaluating carotid atherosclerotic stenosis are ultrasound and, when considering carotid endarterectomy, Magnetic Resonance Angiography (MRA), conventional angiography, or Computed Tomography Angiography (CTA) is performed. The only method used to assess the need for endarterectomy is a measurement of the degree of stenosis [5]. This is a flawed method as the degree of stenosis cannot be used as a marker for plaques with high rupture risk. [6, 7]. Markers such as large Lipid-Rich Necrotic Core (LRNC), Inta Plaque Hemorrhage (IPH), thin fibrous cap, fibrosis, necrotic tissue, inflammation, amount and location of calcification are more relevant in evaluating rupture-prone plaques [8, 9].

All mentioned modalities have drawbacks when it comes to identifying these markers. Ultrasound is challenging to use if the plaque is rich in calcium, if there are varicose (twisted and enlarged) arteries, or if the patient has a short neck. MRA is sensitive to motion artifacts and hemodynamic effects. Conventional angiography should not be used on asymptomatic patients as it can cause the plaque to rupture inducing a TIA or an ischaemic stroke in the patients [5]. The CTA, which is performed on a conventional Computed Tomography (CT), has limited soft tissue resolution and is sensitive to calcium blooming artifacts which can lead to an underestimation of important risk markers and overestimation of stenosis in heavily calcified plaques [10, 11].

Photon Counting Computed Tomography (PCCT) has the potential to perform better in carotid plaque imaging because of the higher spatial resolution, nose reduction, material decomposition and the possibility of creating Virtual Monoenergetic Image (VMI). The noise reduction could lead to an increased contrast in regard to the Contrast to Noise Ratio (CNR). The higher spatial resolution will decrease partial volume effects, which is the main reason for the calcium blooming artifact. Material decomposition can remove calcium and contrast from the image and also decrease beam hardening artifacts. The creation of VMI could provide images with improved soft tissue resolution and more accurately relate the image CT numbers to the tissue type [12].

1.1 Aim

The aim of this project is to investigate if the PCCT images can differentiate materials in carotid atherosclerotic stenosis (*ex vivo* and *in vivo*), by using histopathological images as a reference.

2 Theory

2.1 Computed tomography fundamentals

All CT systems utilize the attenuation of X-ray photons to create images of patients' internal morphology and pathology. In the diagnostic energy range, three different photon interactions are possible: photoelectric effect, Compton scattering, and coherent scattering. The last interaction type contributes negligibly to the photon attenuation when compared to the photoelectric effect and Compton scattering. The coherent scattering will thus be omitted going forward. The photoelectric effect is the dominating interaction at low photon energies and in materials with the high effective atomic number (Z_{eff}). The probability of photoelectric effect interactions will decrease with increasing energy. Compton scattering is relatively independent of Z_{eff} and only increases moderately with increasing photon energy in the diagnostic energy range [12, 13].

The image produced by the CT system represents the attenuation of X-ray photons in the depicted volume. The degree of attenuation in each image pixel is expressed in CT numbers which are assigned to the image pixels during image reconstruction, and are expressed in HU. The CT number depends on the energy of the incoming x-ray photons, Z_eff, and the density of the materials that the photons traverse [14, 15]. The definition of CT-number is shown in the equation below

$$HU(E) = 1000 \cdot \frac{\mu(E) - \mu_{water}(E)}{\mu_{water}(E) - \mu_{air}(E)}, \tag{1}$$

where $\mu(E)$ [cm^{-1}] is the attenuation coefficient as a function of energy, E, of the x-ray photons, $\mu_{water}(E)$ [cm^{-1}] is the attenuation coefficient of water and $\mu_{air}(E)$ [cm^{-1}] is the attenuation coefficient of air [15, 16]. When using a quantity that is closely related to physical property, it becomes possible to identify materials because attenuation depends on material-specific properties. However, two pixels containing different materials could be assigned the same CT number if the materials have similar Z_{eff} or when one material has high Z_{eff} and the other has high density (ρ) [17].

2.1.1 Computed tomography basics

CT systems use one X-ray tube, or two in some cases, as their radiation source. The tube produces an X-ray by accelerating electrons with high voltage from a filament (cathode) into a rotating (for cooling) target (anode). When the electrons collide with the target heat, characteristic X-rays and bremsstrahlung are created. The peak energy ($\mathrm{keV_p}$) of the spectrum is determined by the tube voltage (kV) and the intensity of the spectrum is determined by the tube current (mA). The low energy part of the spectrum consists of photons that will be absorbed in the patient and do not contribute to image information, the low energy part is therefore filtered away to minimize the patient radiation dose [18].
The x-ray beam intensity and size are adjusted to the patient by using a bow-tie filter and collimators respectively. An anti-scatter grid is mounted on the detector to prevent detection of scattered photons which would otherwise degrade the image contrast. The detector and x-ray tube are positioned opposite to each other on a rotating gantry where projections of the patients are collected, where one projection can be seen as a thin planar x-ray image [15, 18].

It is possible to perform image reconstruction of one slice if raw data is collected from projection acquired from little more than half a rotation or from a full rotation. The table is moved along the gantry rotation axis to enable collection of new projections, in the patent volume. There are two main acquisition techniques: the first is "step and shoot" where the gantry only rotates when the table is stationary the second technique is helical or spiral scanning where the table is continuously moved during gantry rotation which results in faster projection acquisition. The width of the image slice is determined by the detector size and the pitch is determined by the beam collimation, p, which is defined as table moment for 360°-rotation divided by the beam collimation. $p < 1$ if the scan volume is irradiated more than once with overlapping beams, resulting in more projection data but also increasing the absorbed dose to the patient. $p = 1$ if all beams are adjacent in the scan volume. $p > 1$ will result in fewer projection data and absorbed dose to the patient due to the beams being separated [18].

2.1.2 Energy integrating detector

Conventional CT systems are equipped with Energy Integrating Detector (EID) which uses indirect conversion when detecting x-ray photons. Incoming X-ray photons are converted into visible light in the scintillation material. The visible light is absorbed in a photodiode, converted into a current, and then shaped into a voltage signal. The amplitude of the voltage signal is proportional to the energy of all incoming X-ray photons during the acquisition time. This implies that the EID does not possess any energy resolution capabilities and low-energy photons will be down-weighed by the integration. Low-energy photons carry the majority of contrast information, so this down-weighing leads to a decreased Contrast Noise Ratio (CNR) in the image. The integration also causes electronic noise to be incorporated into the signal thus decreasing Signal to Noise Ratio (SNR) of the image. The detector elements are separated by a septa to prevent cross-talk but the septa also degrade the geometrical efficiency together with the anti-scatter grid [12–14, 19]. The figure below shows a schematic EID.

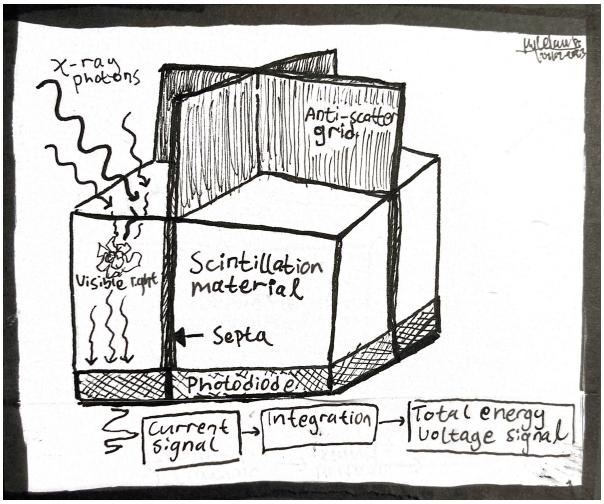

Figure 1: The EID with four detector elements or pixels. Components and a simple flowchart of the signal processing can also be seen in the figure.

2.2 The photon counting computer tomography

2.2.1 Photon-counting detector

The PCCT systems' technical design is similar to that of a conventional CT system, however, a Photon Counting Detector (PCD), is used instead of an EID, which uses direct conversion to detect x-ray photons. The PCD can be made from CdTe (cadmium telluride), CdZnTe (cadmium zinc telluride), or Si (silicon). Cd-based detectors can be made thin due to high atomic number and absorption efficiency while Si-based must be thicker because of the lower atomic number and absorption efficiency. The detection principle remains the same for the different materials, the incoming X-ray photons are absorbed in the semiconducting material, and charge carriers (electron-hole-pairs) are created. The electrons drift towards a pixelated anode due to a voltage bias placed over the detector element. The resulting current signal is shaped into a voltage signal with an amplitude proportional to the absorbed x-ray photon energy. The voltage signal is compared to inbuilt voltages that are calibrated to correspond to different energy thresholds and the detection event is counted if the voltage signal exceeds the energy threshold. This implies that the PCD counts every X-ray photon equally independent of their energy. It is also possible to sort the counted photons into an energy bin if at least two energy thresholds are used. The ability to create energy bins opens up the possibility of producing Virtual Monoenergetic Image (VMI) and performing material decomposition [12, 13].

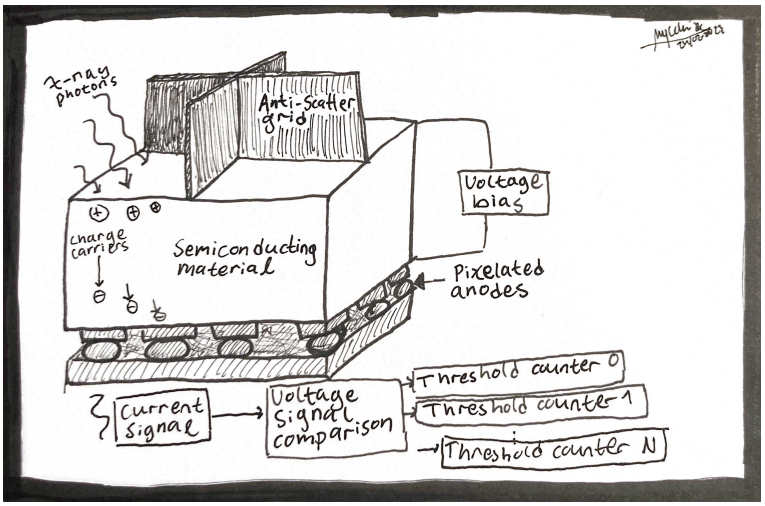

Figure 2: The PCD with four detector elements or pixels. Components and a simple flowchart over the signal processing can also be seen in the figure.

The differences in technical principles behind the PCD when compared to the EID give some implications for the PCD properties. Firstly, the detector elements are only separated by the electrical field, produced by the voltage bias, meaning that only the anti-scatter grid degrades the geometrical efficiency. Secondly, the detector elements are divided into macro pixels (macro mode) by the anti-scatter grid. However, it is possible to further divide the macro pixels into subpixels which improves the spatial resolution. This mode is called Ultra-High Resolution (UHR). Thirdly, the electronic noise can be removed by placing the lower energy threshold above the electronic noise (around 20 keV) which means that the raw data used for tomographic reconstruction will be void of quantum noise. Also, by weighing the lower energy bin heavier the CNR can be

improved, at the cost of increasing beam hardening artifacts [12, 13, 19, 20]. The figure shows typical X-ray energy spectra with marked thresholds.

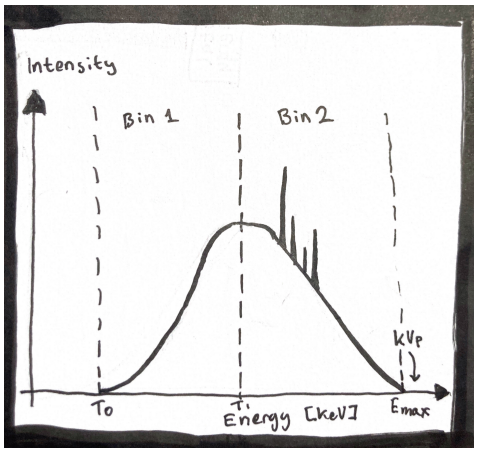

Figure 3: The counted photons are divided by two thresholds. T_0 is placed above the electronic noise and every photon up to E_{max} will be counted into this group. Likewise every x-ray photon with energy T_1 ut to E_{max} will be counted as another group. The energy bins is calculated as follows Bin $1 = T_0 - T_1$ and Bin $2 = T_1$.

2.2.2 Photon counting detector limitations

The PCD also has limitations due to its design. In Si-based detectors, the dominating photon interaction is Compton scattering, due to its low atomic number. An incoming X-ray photon may deposit some of its energy in one detector element only to scatter and deposit the rest of its' energy in a neighboring element. Compton scattering is more uncommon in Cd-based detectors, due to the higher atomic number, however, both Cd and Te have their K-edges within the diagnostic energy range meaning that an incoming x-ray photon could kick out a K-shell electron of the detector material. The created vacancy is refilled and in the process, a characteristic x-ray photon is released which can be absorbed in another detector element, this so-called k-escape. A third event called charge sharing happens when an incoming X-ray photon is absorbed close to the border of two detector elements. The created charge carriers are split between the two detector elements. Compton scatter reabsorption in neighboring elements, k-escape, and charge sharing result in one high energy photon being registered more than once at the wrong energy, thus leading to degraded spectral separation, energy resolution, and spatial resolution [12, 19].

The PCD could express another limitation called pile-up at higher dose rates. When the dose rate is high, two or more incoming X-ray photons are simultaneously absorbed in one detector element. This results in the photons being counted as one and a voltage signal with an amplitude that corresponds to the sum of the photon energies. Even an overlap of two voltage signals will cause incorrect registration of energy. Pile-up causes the SNR to decrease because fewer photons are counted and the energy resolution will degrade. Furthermore, the degradation of image quality will be concentrated in tissues with low attenuation where the dose rate to the detector is highest. It is possible to reduce the effects of pile-up by using smaller pixels because fewer photons will be able to be absorbed at the same time in one detector element, however, smaller pixels will increase the probability of Compton scatting, k-escape, and charge sharing [12, 19, 21].

2.3 Image reconstruction

The raw data collected by the PCCT system differs from the data from CT system. The image reconstruction of PCCT-data must be performed differently and the clinically used reconstruction method is called Quantum Iterative Reconstruction (QIR), from Siemens Healthineers. QIR corrects for geometrical cone beam artifacts and beam hardening artifacts and reduces noise. The reconstruction method is not based purely on Filtered Back Projection (FBP) but also utilizes Iterative Reconstruction (IR) methods to remove noise and artifacts [20, 22].

2.3.1 Filtered back projection

The number of photons in the X-ray beam decreases exponentially as it traverses the patient, due to the photons interacting with matter within the patient. The number of photons that reach the detector, $I(x)$, can be expressed with Beer–Lambert's law

$$I(x) = I_0 \cdot e^{-\int_{path} \mu_z(x,y)dy}, \tag{2}$$

where I_0 is the number of photons emitted by the x-ray tube and $\mu_z(x, y)dy$ is the distribution of attenuation coefficient at a patient slice z. The projection along the x-axis consists of line integrals along the path that the x-ray photons that have traversed the patient, in this case, parallel to the y-axis. The raw data consist thus of several projections that are collected at different angles. The resulting projection of the attenuation coefficient along t at angel θ is expressed as

$$p(t, \theta) = \ln\left(\frac{I}{I_0}\right) = \int_{path} \mu_z(x, y)ds, \tag{3}$$

where ds is a dummy variable that indicates the line integral orientation which is always parallel to the x-ray beam. The collected projections can be presented in a sinogram where the x-axis is $p(t, \theta)$ and the y-axis is θ. As mentioned before, projections must be collected from little more than a half or a full rotation to make image reconstruction possible. The figure below shows a schematic principle of projection collection and the resulting sinogram.

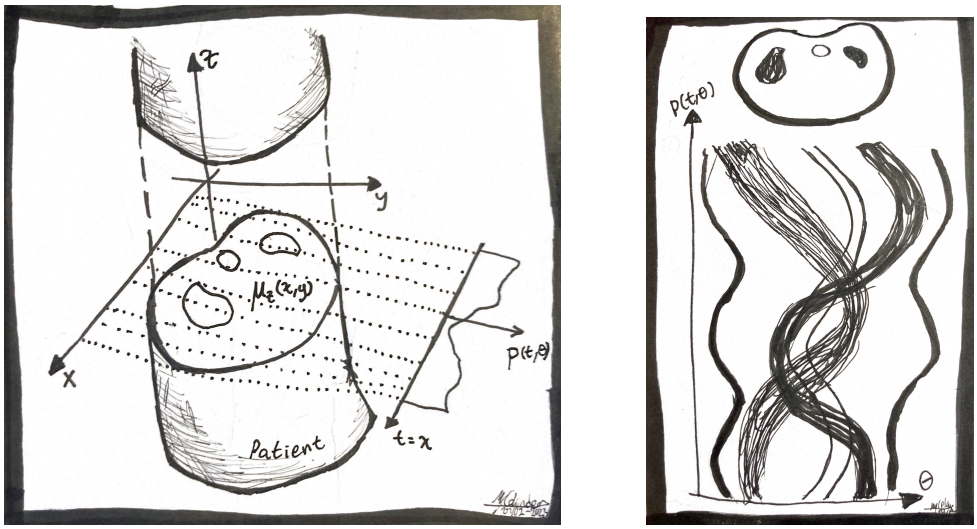

(a) **(b)**

Figure 4: The resulting projection along the x-axis of a patient slice with the distribution of attenuation coefficients, $\mu_z(x, y)dy$. The dotted lines represent the line integrals. Figure 4b show the resulting sinogram of the patient slice when the projections were acquired for a full rotation.

The principle behind normal Back Projection (BP) is that the projections are redistributed across an image array for all angles. This is done practically by dividing the attenuation values in the sinogram by the number of image pixels that would represent the X-ray beam path for each angle, all projections contribute equally to the image. The resulting image however will be blurred because BP will allocate the spatial projection data across the image array. This blurring can be corrected by applying a filter or a kernel to the projections before BP is performed. Take the ramp filter, which belongs to the family of Sharp filters, as an example. A Sharp filter is designed to weigh high frequencies heavier, which will amplify edges and details leading to an improved spatial resolution in the image. But it will also increase the noise level. Furthermore, the increased noise will make it more difficult to see low-contrast objects. There are also soft filters that reduce the image noise but this results in less defined edges of objects in the image which impairs the visualization of high-contrast objects. It is called FBP if a filter is involved in the BP image reconstruction [18, 23, 24].

2.3.2 Iterative reconstruction

The principle of an iterative process can be described as a task that is performed several times where the previous result is accounted for in the next iteration. The process will repeat until maximum iterations have been performed or some other criterion is reached. In the case of image reconstruction, a possible iteration process cycle would consist of the following steps:

1. The synthesized projections, based on a real image that consisted of measured projections that has undergone FBP, are created via forward projection
2. the synthesized and measured projections are compared and a correction term is calculated based on the found difference between the projections
3. FBP is performed on the real projections after the correction term have been applied

4. the step 1 through 3 are repeated until the desired result is met.

The creation of synthesized projections requires a model of how the PCCT system reconstructs images. The model often includes system optics and system statistics where system optics refers to the system geometry which includes the distance between the x-ray tube, isocenter, and detector, its components such as shape and size of the focal point and the detector elements, and even the beam and detector geometry. System statistics refers to emitted photon spectrum, the statistical distribution of photons, and the noise from electronics. Modeling system optics will increase spatial resolution while modeling system statistics will reduce image noise. The commercially available IR algorithms can be classified into two categories: statistical (or hybrid) IR and Model-Based Iterative Reconstruction (MBIR). Statistical IR is used in both image and projection space to reduce image noise while MBIR is used to improve spatial resolution of the image [23].

Statistical IR filters data in both projection space and image space and the method transition between projection and image space by using normal FBP. The iterative filtration in projection space analyses the variation of data with statistical models where neighboring projection data is compared with the goal of identifying projections with low SNR. The identity is then replaced or modified to achieve minimal variation, furthermore, the different projections can be given different weights enabling projections with higher SNR to contribute more to the image. In image space, after FBP is performed, image data is once more iteratively filtered by using statistical models to remove expected noise in body structures. Lastly, a Sharp filter is often added to preserve edges and detail in the image. Note that no new data is added in projection or image space which means that the method only removes noise without affecting the image quality [16, 23].

MBIR models the PCCT-systems imaging process, an estimate of the object (a prior), and noise in the projection data. Iteration begins with an FBP of an artificial image of the object created from modeled data. The projections are created from the artificial image via forward projection where information from a prior and models of the system imaging process are accounted for. The artificial projection is compared with the measured projection and a correction term is calculated based on the object and noise models. FBP is performed on the corrected projections and the interactive process repeats until the correction term becomes negligible. The MBIR can reduce image artifacts if the system imaging process is modeled correctly and in the ideal case image noise can simply be removed from the projections in the last iterative step [16, 23].

2.3.3 Material decomposition

By performing material decomposition the full energy dependence of the attenuation coefficient function in every voxel is determined. There is no need to measure the attenuation coefficient in a large number of energy bins because human tissue can approximately be described as a linear combination of two basic materials, this will be shown mathematically later in this section, thus only two bins are needed to extract the information where more bins will not add new information about the tissue.

Material decomposition utilizes the attenuation coefficient dependence of the photoelectric effect and Compton scattering to determine the material components of a tissue.

The attenuation coefficient as a function of energy is linear for all naturally occurring materials in the human body and can be expressed as a linear combination of the photoelectric effect and Compton scattering interactions. When the photon interactions are expressed as effective atomic number (Z_{eff}) and density (ρ) a $Z_{eff}\rho$ map can be produced where material information can be extracted. The following equation shows the attenuation coefficient of a material as a function of energy, expressed with the photon interactions

$$\mu(E) = \rho \cdot \left[\left(\frac{\mu}{\rho}_{PE}(E, Z) \right) + \left(\frac{\mu}{\rho}_{CS}(E, Z) \right) \right] \approx \tag{4}$$

$$\approx \rho \cdot \left(\alpha \cdot \frac{Z_{eff}^k}{E^n} + \beta \cdot f_{KN}(E) \right) \Rightarrow \tag{5}$$

$$\Rightarrow \left(\frac{\mu}{\rho} \right)(E) = \alpha f_{PE}(E) + \beta f_{CS}(E), \tag{6}$$

where ρ is the density of the material, $f(E)_{PE}\frac{Z_{eff}^k}{E^n}$ describes the attenuation caused by the photoelectric effect where $k \sim 3-4$ and $n \sim 3-3.5$. furthermore $f(E)_{CS} = f_{KN}(E)$ is the Klein-Nishina function and describes the attenuation due to Compton scattering, note that the function only weakly depends on energy. α and β are constants that represent the energy-independent contribution from the photoelectric effect and Compton scattering. It is possible to determine α and β by using the energy-resolving ability of the PCCT system. The information from two energy bins creates the following solvable equation system

$$\begin{cases} \left(\frac{\mu}{\rho} \right)(E_L) = \alpha f_{PE}(E_L) + \beta f_{CS}(E_L) \\ \left(\frac{\mu}{\rho} \right)(E_H) = \alpha f_{PE}(E_H) + \beta f_{CS}(E_H), \end{cases} \tag{7}$$

where E_L and E_H denote information collected from the low energy bin and high energy bin respectively in the x-ray spectra. When solving the equation system each material can be unlike represented by (α, β). Material decomposition is then performed by replacing $f_{PE}(E)$ and $f_{CS}(E)$ with the mass attenuation coefficient functions $\left(\frac{\mu}{\rho} \right)_A(E)$ and $\left(\frac{\mu}{\rho} \right)_B(E)$ from the basis materials A and B. For two basis materials equation 6 becomes

$$\left(\frac{\mu}{\rho} \right)_A(E) = \alpha_A f_p(E) + \beta_A f_c(E) \text{ and} \tag{8}$$

$$\left(\frac{\mu}{\rho} \right)_B(E) = \alpha_B f_p(E) + \beta_B f_c(E), \tag{9}$$

where α_A, α_B, β_A, and β_B represent the contributions from the photoelectric effect and Compton scattering for materials A and B respectively. When solving for $f_{PE}(E)$ and $f_{CS}(E)$ and inserting the result into equation 6 again the following equation is extracted

$$\left(\frac{\mu}{\rho}\right)(E) = \frac{\alpha\beta_B - \alpha_B\beta}{\alpha_A\beta_B - \alpha_B\beta_A}\left(\frac{\mu}{\rho}\right)_A(E) + \frac{\alpha_A\beta - \alpha\beta_A}{\alpha_A\beta_B - \alpha_B\beta_A}\left(\frac{\mu}{\rho}\right)_B(E) = \tag{10}$$

$$= \xi_A\left(\frac{\mu}{\rho}\right)_A(E) + \xi_B\left(\frac{\mu}{\rho}\right)_B(E), \tag{11}$$

where ξ_A and ξ_B are energy independent. Equation 11 also shows that the linear mass attenuation coefficient of composite material can be expressed as a linear combination of mass attenuation coefficient for two basis materials with sufficiently different attenuation properties (such as water and calcium). When energy information from low and high energy bins are available and both sides in equation 11 is multiplied with the mass density ρ and the following are given

$$\begin{cases} \mu(E_L) = \xi_A\rho\left(\frac{\mu}{\rho}\right)_A(E_L) + \xi_B\rho\left(\frac{\mu}{\rho}\right)_B(E_L) = \\ = \rho_A\left(\frac{\mu}{\rho}\right)_A(E_L) + \rho_B\left(\frac{\mu}{\rho}\right)_B(E_L) \\ \mu(E_H) = \xi_A\rho\left(\frac{\mu}{\rho}\right)_A(E_H) + \xi_B\rho\left(\frac{\mu}{\rho}\right)_B(E_H) = \\ = \rho_A\left(\frac{\mu}{\rho}\right)_A(E_H) + \rho_B\left(\frac{\mu}{\rho}\right)_B(E_H), \end{cases} \tag{12}$$

and equation 12 is solved for every pixel which gives images over the mass densities of the materials A and B. Material decomposition can be performed in both image and projection space. The prospects of performing material decomposition in projection space are that effects from artifacts such as beam hardening can be avoided by implementing models that consider how the x-ray spectra change before it is detected. The overall accuracy of the decomposition will be degraded if beam hardening artifacts are not addressed. The accuracy could also be degraded if the raw data is noisy or if the decomposition is performed in image space with noisy images [12, 17, 19, 21].

2.3.4 Virtual monoenergetic images

It is possible to produce VMI with the energy resolution capabilities of the PCCT system. The VMI has the appearance of an X-ray image acquired with monoenergetic X-ray photons and photon energy information from two energy bins is sufficient when creating a VMI. It is possible to generate VMI at any energy however it is only practical to do it within the diagnostic energy range of $40 - 200$ keV. There are a number of different methods to create VMI: one method is to use the ρ_A and ρ_B found with material decomposition and use equation 12 to produce an image at some preferred energy E_m according to

$$\mu(E_m) = \rho_A\left(\frac{\mu}{\rho}\right)_A(E_m) + \rho_B\left(\frac{\mu}{\rho}\right)_B(E_m), \tag{13}$$

where $\left(\frac{\mu}{\rho}\right)_A(E_m)$ and $\left(\frac{\mu}{\rho}\right)_B(E_m)$ is the mass attenuation coefficients at energy E_m. Another possible method to produce a VMI is by using the weighted sum of low and high-energy images with

$$CT(E_m) = w(E_m)CT_L + (1 - w(E_m))CT_H, \tag{14}$$

where CT is the CT number for the low and high-energy images respectively and $w(E_m)$ is the weighting factor that depends on the desired monoenergetic energy and the effective engines of the low and high-energy acquisition. A third method of creating monochromatic images is similar to material decomposition where the contributions from the photoelectric effect and Compton scattering are used as follows

$$\mu(E_m) = (\rho_{PE})f_{PE}(E_m) + (\rho_{CE})f_{CE}(E_m), \tag{15}$$

where $f_{PE}(E_m)$ and $f_{CE}(E_m)$ are functions that describe the photoelectric effect and the Compton scattering mass attenuation coefficients respectively and ρ_{PE} and ρ_{CS} are associated mass densities which are determined from material decomposition. The last method performs material decomposition and produces VMI in projection space where a basis sinograms of ρ_A and ρ_B from equation 12 or ρ_{PE} and ρ_{CS} from equation 15 are generated. With the sinograms, it becomes possible to reconstruct basis material mass density images and thus convert them into monoenergetic images similar to equation 13 or 15. Furthermore, there is also a possibility to directly convert the basis sinograms into a sinogram of a monoenergetic image at energy E_m by using

$$P\left[\mu(E_m)\right] = P\left[\rho_A\right]\left(\frac{\mu}{\rho}\right)_A(E_m) + P\left[\rho_B\right]\left(\frac{\mu}{\rho}\right)_B(E_m), \tag{16}$$

where $P\left[\mu(E_m)\right]$ is the monoenergetic sinogram and an image is produced by performing FBP [17, 19, 21].

2.4 Calcium blooming artefacts

Calcium blooming artifacts are one of the main reasons for inaccurate evaluation of the degree of stenosis in highly calcified plaques and it can cause underestimation of soft materials (lipid, necrotic, fibrous, thrombus etc) in the plaque. The root causes of calcium blooming artifacts are motion artifacts caused by fast motions, such as pulsating blood, and partial volume effect which depends on the system's spatial resolution and image reconstruction. Both artifacts cause image blurring but the partial volume effect also encompasses when an object is assigned the wrong CT number due to only being partly inside the image slice. Motion artifacts can be effectively reduced by algorithms in motion reduction software or by using ECG-triggering. The partial volume effect can be reduced by using detectors with small detector elements, image reconstruction with in-built edge preserving *prior* of the calcium, material decomposition which can remove the calcium, and post-processing techniques such as deep learning which is trained to sharpen edges of calcium [25].

2.5 Carotid Atherosclerotic Plaque

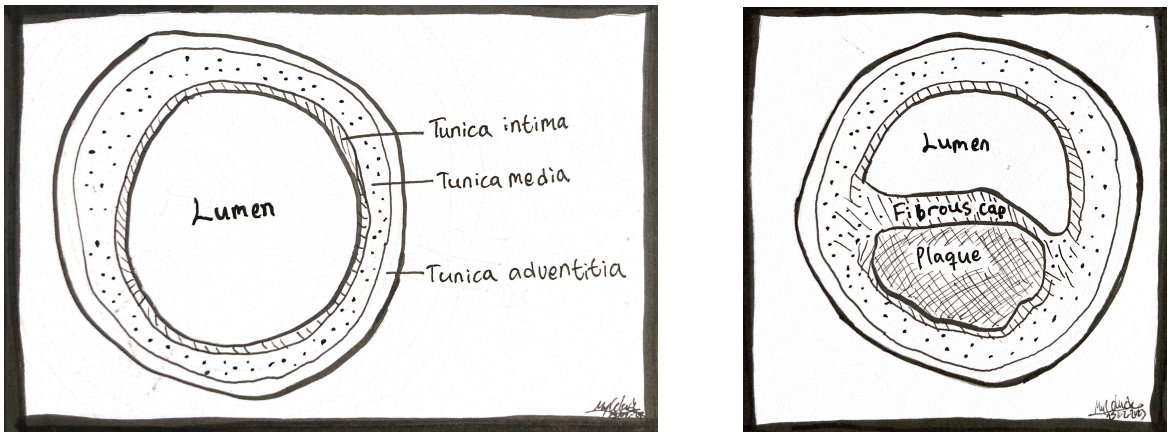

(a) **(b)**

Figure 5: Cross section of a healthy artery without any occlusions. The artery consists of a lumen, where blood flows. The artery wall is divided into three parts: Tunica intima, Tunica media, and Tunica adventitia. Tunica intima consists of fine connective tissue and elastic fibers arranged in a net-like structure. Tunica media mainly consist of smooth muscle cells and elastic fibers arranged in spirals. Lastly, Tunica adventitia consists of supportive collagen fibers. Figure 5b shows an occlusion of the artery due to plaque formation inside the Tunica intima. The only structure that separates the plaque from the lumen is the thin fibrous cap [7, 26].

Carotid atherosclerosis is a disease where thickening and loss of elasticity of the Internal Carotid Artery (ICA), the External Carotid Artery (ECA), or Common Carotid Artery (CCA) wall occurs. The wall thickening is caused by plaque formation inside of the innermost layer artery wall (tunica media), see figure 5, where the plaque often consists of fatty lesions, calcifications and a fibrous cap that separates the plaque from the artery lumen. Carotid atherosclerosis is known to cause TIA and stroke. Today only the degree of stenosis, or occlusion, of the carotid lumen is used to evaluate the eligibility to perform carotid endarterectomy (removal of plaque in the arterial wall), where the patient will benefit from surgery if there is an occlusion of $> 50\%$ of vessel lumen [5, 27, 28].

Three methods have been used to measure the degree of stenosis: the European Carotid Surgery Trial (ECST)-method, the North American Symptomatic Carotid Endarterectomy Trial (NASCET)-method, and the Common Carotid (CC)-method. The NASCET, ECST, and CC methods calculate the degree of stenosis, DS according to the following equation [29]

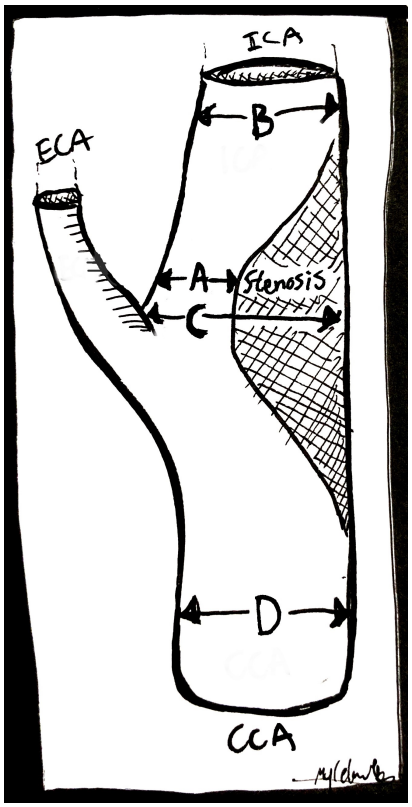

Figure 6: The carotid artery, where the ICA, the ECA and CCA is visible. The shadowed part denotes stenosis and the different variables A, B, C and D are distances used to evaluate the degree of stenosis depending on the preferred method, see equation 17.

$$DS_{\text{NASCET}} = \frac{B - A}{B} \tag{17a}$$

$$DS_{\text{ECST}} = \frac{C - A}{C} \tag{17b}$$

$$DS_{\text{CC}} = \frac{D - A}{D} \tag{17c}$$

It has been observed that ischemic events do not only occur due to carotid occlusions, which limit the flow of blood but also arterial emboli from thrombus formation caused by rupture of the fibrous cap. Plaque that has a risk of rupturing is called vulnerable plaque. These plaques are characterized by a large lipid-rich necrotic core, Intra Plaque Hemorrhage (IPH), a thin fibrous cap from extracellular matrix degradation and depletion of smooth muscle cells, inflammation, and generally lacking calcification. But the role of calcification being plaque stabilizing is uncertain because the calcification can vary greatly in amount, size, shape, and position. The irregular surface of the arterial wall is associated with rupture and can be identified with contrast medium seemingly breaching the luminal wall. It is however hard to identify in conventional CT images due to the similarities in luminal contrast and calcification attenuation [8, 9, 30]. It is of outermost interest to investigate if the PCCT system can identify markers for vulnerability or stability of the plaque as the identification of these markers could be of high clinical value when evaluating the best treatment for the patient.

3 Materials and method

3.1 Patient selection, sample preparation, and histopathology

A patient who was a candidate for carotid endarterectomy was the focus of this study. The patient was remitted for a CT scan to evaluate the degree of stenosis caused by a carotid atherosclerotic plaque.
The patient was scanned in the PCCT and carotid endarterectomy was performed afterwards. The removed plaque had to be divided into two parts: one located in the CCA near the carotid bifurcation and the other located in the ICA. Directly after the surgery, the plaque was frozen, dried, and embedded in paraffin. The *ex vivo* carotid plaque was scanned in the PCCT. Figure 7 show the setup of the *ex vivo* plaque for the PCCT scan.

This study is part of a project that was approved by the Ethical Committee (Dnr 472/2005). The patient received oral and written information about the study and agreed to participate. The patient also agreed to have the surgically removed plaque saved in a biobank.

Figure 7: The plaque part to the left is a plaque from Internal Carotid Artery (ICA) and the plaque part to the right is a plaque from the bifurcation. The rubber band and the wrapped candy was used as references to locate the plaque parts in the acquired PCCT images.

To prepare for histopathological analyzes, the plaque was sectioned first into slabs, around 0.5 mm thick, and then into thin slices, 5 μm. Different staining methods were used to visualize components typical for vulnerable plaques. The methods used in this project were Van Cossa (calcifications), Movat (general staining), CD68 (macrophages),

and SMC (smooth muscle cells). The thin slices were scanned in a digital slide scanner creating high-resolution color images of the histopathology of the plaque slices.
From the histopathological images of the *ex vivo* plaque, slices containing interesting materials (markers for vulnerable plaque) were identified. The interesting materials which could be identified were calcium, fibrosis, inflammation, IPH/bleeding, and thrombus. Note that there are more rupture markers that could be identified but these were excluded due to the minor abundance in the interesting slices. There were nine interesting slices in total, five in ICA and four in the CCA near the carotid bifurcation. The location of the interesting slices can be seen in the schematic figure 8.

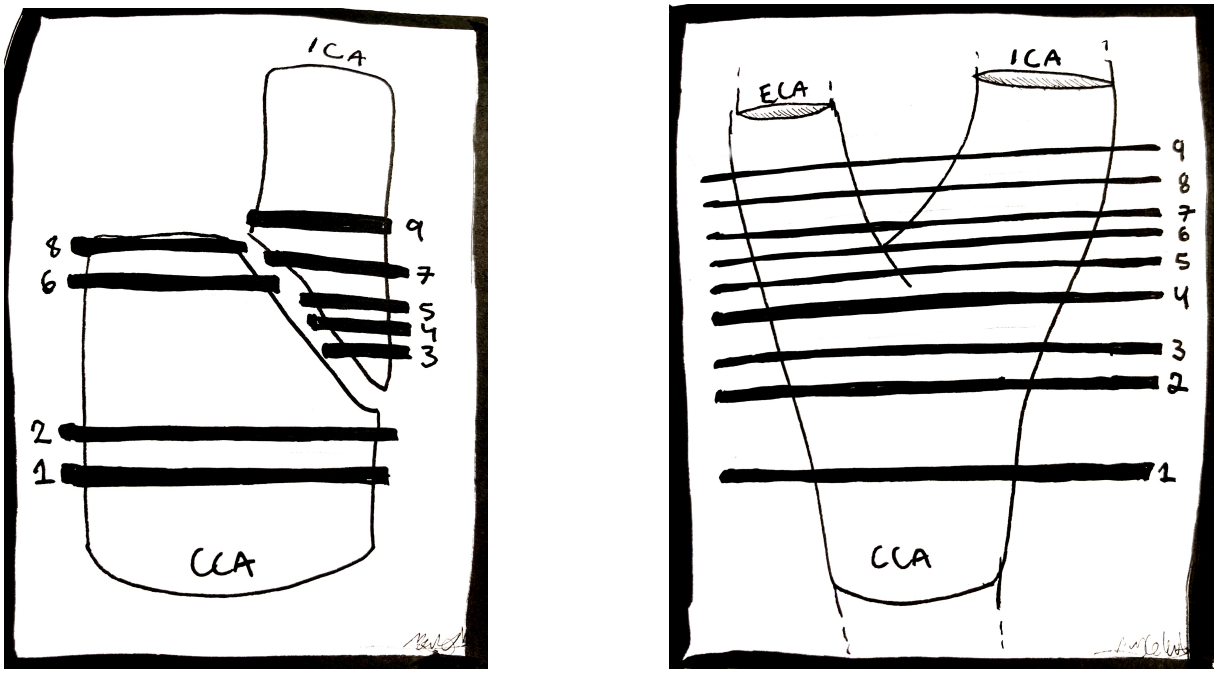

(a) **(b)**

Figure 8: The schematic figure 8a shows the location of the interesting slices in the two plaque parts. Figure 8b show the corresponding slice locations *in vivo*.

3.2 Imaging modality

3.2.1 PCCT imaging

The PCCT used during this study was NAEOTOM Alpha (Siemens Healthineers, Erlangen, Germany). The system consists of two tube-detector pairs where the tube type is Vectron^{TM} and the detector type is QuantaMax^{TM}. The detectors are CdTe-based and have a pixel size 0.4×0.4 mm^2 and in UHR-mode the minimum detector subpixel size is 0.2×0.2 mm^2. Furthermore, the lowest energy threshold is set to 20 keV to eliminate electronic noise [20]. The PCCT software used when acquiring images of the patient (*in vivo*) and the surgically removed plaque (*ex vivo*) was syngo CT VA50A.

The *in vivo* scan was performed in UHR mode, without and with contrast medium (Omnipaque 350 mg Iodine/ml, 60 ml) followed by saline (50 ml) according to standard clinical procedures. The *ex vivo* scan was performed with a higher radiation dose. Table 1 show the scan parameters used for the acquisitions.

Table 1: The scan parameters used on the PCCT for the acquisition of the *ex vivo* and *in vivo* images.

Parameter	*In vivo*-with contrast medium	*Ex vivo*
Tube voltage [kV]	120	120
Effective tube current [mAs]	170	247
Pitch	0.85	0.85
Rotation time [s]	0.5	0.5
Collimation [mm]	120×0.2	120×0.2
CARE Dose4D and CARE keV	Full	Full
CARE keV IQ	150	400
CARE keV Optimized for	Vascular	Non-contrast
$CTDI_{vol}$ (32 cm) [mGy]	13.60	19.90
Matrix size	1024×1024	1024×1024
Filter	Hv64	Hv64

After acquiring the raw data, several images were reconstructed in the PCCT system. VMI was reconstructed from 40 to 190 keV, in steps of 10 keV. The images had a slice thickness of 0.40 mm. Energy-integrated images were also reconstructed with the slice thickness of 0.2 mm.

3.2.2 Conventional CT imaging

The patient was examined on a conventional CT system three days prior to the PCCT scan. This enables visual comparison of the plaque, *in vivo*, on both modalities. The conventional CT images of the patient were acquired with the Dual-Energy Computed Tomography (DECT) SOMATOM Definition Flash (Siemens Healthineers, Erlangen, Germany). The dual-energy acquisition mode was disabled, thus creating conventional energy-integrated images. The images were reconstructed in the software, version number syngo CT VB20A. Table 2 show the parameters for the acquisition.

Table 2: The scan and reconstruction parameters used for the *in vivo* images on conventional CT.

Parameter	*In vivo*-with contrast medium
Tube voltage [kV]	100
Effective tube current [mAs]	286
Pitch	0.6
Rotation time [s]	0.33
Collimation [mm]	64×0.6
Quality ref mAs	400
$CTDI_{vol}$ (32 cm) [mGy]	11.78
Matrix size	512×512
Slice thickness	0.6 mm
Filter	Bv40f/3

3.3 Analysis of reconstructed images

The *ex vivo* and *in vivo* reconstructed images were analyzed in *syngo.via* (software version VB60A_HF03). ROIs were used to measure the mean CT number of the interesting materials. The histopathological images were used to correctly place the ROIs. If there were uncertainties of material content in the histopathological images ROIs in those locations were excluded from the analysis. To reduce the number of measurements, but include a wide range of energies, VMI of 40, 50, 60,... 190 keV was used. The energy-integrated image with a slice thickness of 0.2 mm was used to help with the localization of the interesting slices, see figure 8.

The *ex vivo* ICA plaque part appears much longer when compared to the corresponding anatomy *in vivo*, this is due to the technique used during the carotid endarterectomy. This causes a visual overlap between *ex vivo* and *in vivo* images when trying to identify the same slices in the *in vivo* images, as in the *ex vivo* images. Figure 9 show how the ICA plaque is divided from the rest of the carotid artery during surgery.

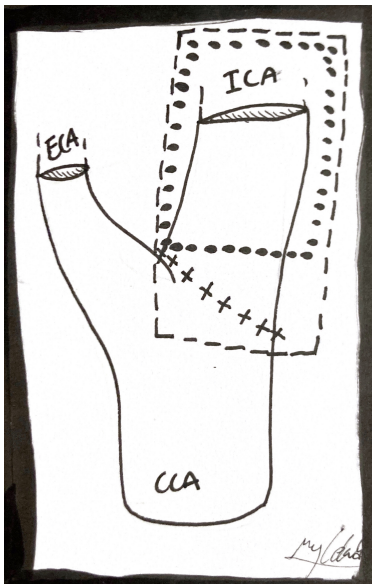

Figure 9: The figure shows the carotid artery and its components Common Carotid Artery (CCA), External Carotid Artery (ECA), and Internal Carotid Artery (ICA). During surgery, the plaque segment inside ICA is removed according to the line marked with plus signs. This means that the ICA will be interpreted as longer in the *ex vivo* PCCT images, denoted with dashed lines - compared to the *in vivo* PCCT images - denoted with dotted lines.

3.4 Regions of interest

Figure 10a presents an example (slice 6, near the bifurcation of the carotid artery) of how ROIs were placed, all slices can be seen in the appendix. ROIs are colored according to their material content, red for calcium, orange for fibrosis, green for inflammation, blue for IPH/bleeding, and purple for thrombus. The placement of the ROIs in the *ex vivo* (10b) and *in vivo* (10c) image is made using the corresponding histopathological image (10a).

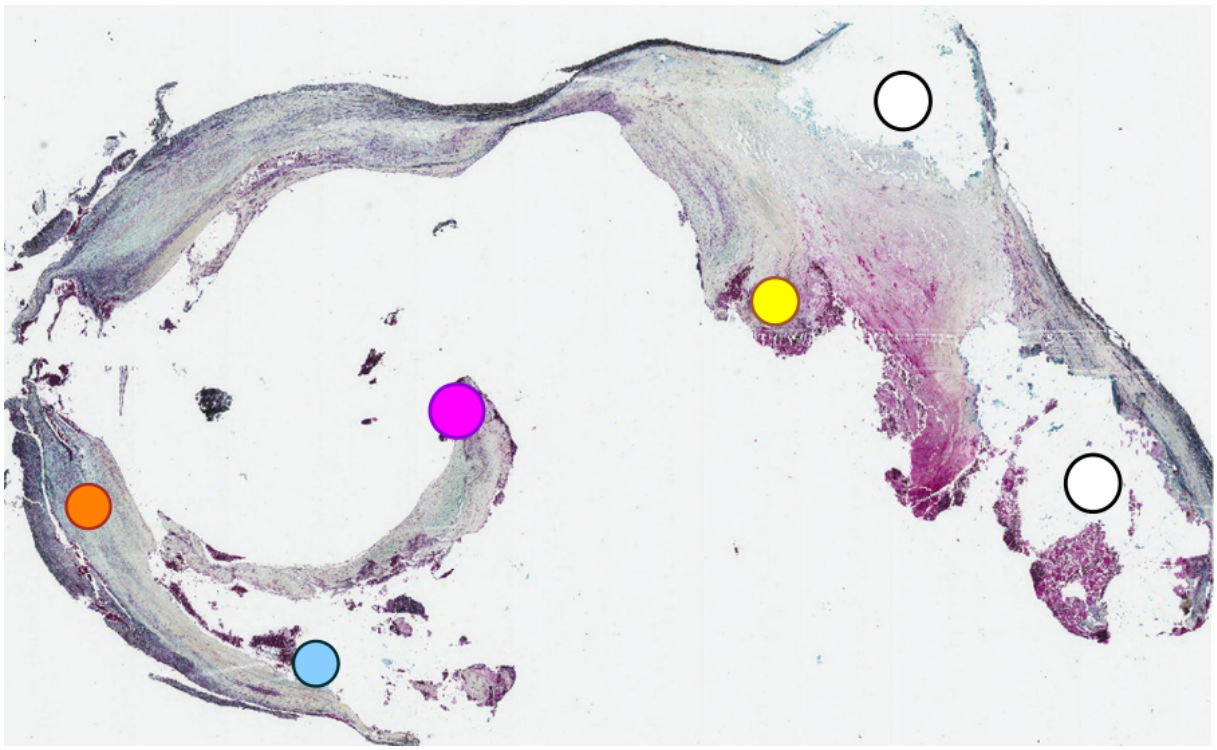

(a)

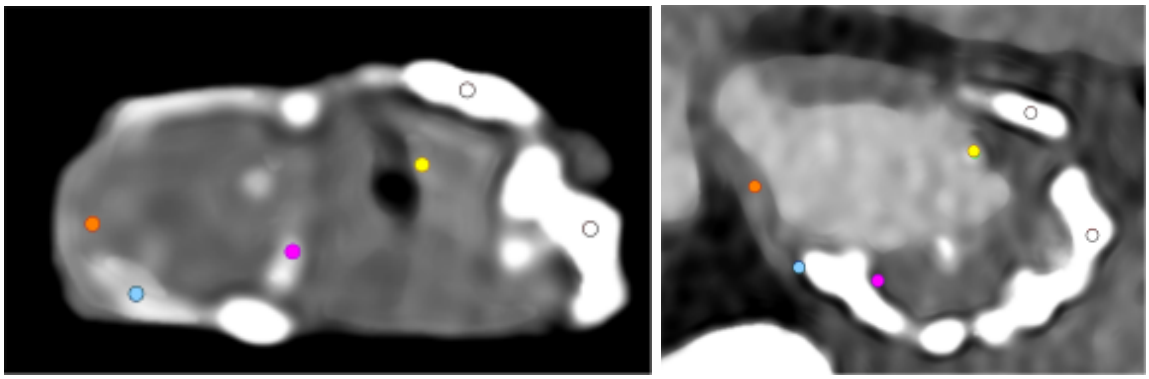

(b) (c)

Figure 10: The histopathological (10a) and PCCT images (slice 6), *ex vivo* (10b) and *in vivo* (10c). ROI colors define the material content according to the histopathological analysis. white- calcium, orange - fibrosis, yellow - inflammation, blue - IPH/bleeding, magenta - thrombus.

Table 3: The total number of ROIs identified for each material overall interesting slices in the *ex vivo* and *in vivo* images.

Image/ Material	Calcium	Fibrosis	Inflammation	IPH/bleeding	Thrombus
Ex vivo	16	10	5	13	3
In vivo	15	9	3	11	3

The number of identified ROIs found in the *ex vivo* and *in vivo* images varies depending on the material. This variation is due to the possibility of comparing the materials identified by the histopathology with the structures in the *ex vivo* and *in vivo* images.

3.5 Statistic tests

The one-way ANOVA test was used to determine if there was any significant difference between the mean CT number of the materials. The null hypothesis is that there are no differences between the mean CT number of each material. One-way ANOVA was performed on the measurements from each reconstructed VMI. The study focuses on soft materials with similar CT numbers thus excluding calcium from all statistical tests.

Energy levels with significant differences between materials, according to one-way ANOVA, were further analyzed. Two-sided t-tests (assuming different variances) were performed to determine which materials could be distinguished from each other. Bonferroni correction was used to correct for the increased risk of type I errors (false positives) when doing multiple statistical tests on the same data set. The new p-value becomes $p_{new} = \frac{p}{n_{t-test}}$ where n_{t-test} is the number of t-tests performed. The number of materials used during the two-sided t-test was fibrosis, inflammation IPH/bleeding, and thrombus which makes a total of six statistical tests. The Bonferroni correction gives $\frac{0.05}{6} = 0.0083\overline{333}$

The Confidence Interval (CI) was set to 95% ($p = 0.05$) for one-way ANOVA and it was set to 99% ($p = 0.0083$) after the Bonferroni correction for the t-test. All statistical analyses were performed in *Microsoft Excel*.

4 Results

Figure 11 shows data from the analysis of *ex vivo* scans, including all interesting materials (calcium, fibrosis, inflammation, IPH/bleeding and thrombus). It can be seen that calcium (white) differs from the rest of the materials where its CT numbers decrease with higher energies. The soft materials (fibrosis, inflammation, IPH/bleeding, and thrombus) tend to have higher CT numbers at increasing energy. Soft materials also reach a plateau earlier than calcium.

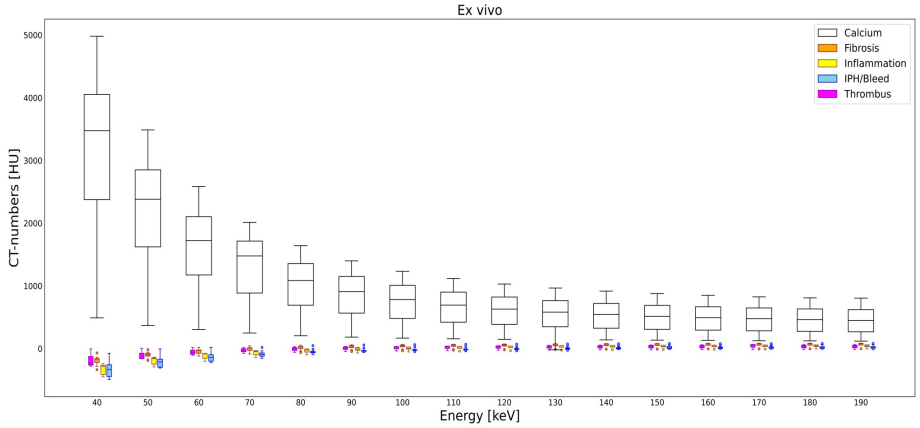

Figure 11: Box plots of the measured *ex vivo* CT numbers- for the chosen ROIs for each reconstructed energy.

To better visualize the soft materials, data from calcium ROI:s was removed. Data is shown in Figure 12. It can be seen in figure 12 that there are outliers of fibrosis (orange) that follow the box plot trend but shifted below the plot. There are also outliers above the box plot but those disappear for energies above 40 keV. Inflammation (yellow) outlier tends to lower CT numbers at higher energies and appears at energies above 100 keV. IPH/ bleeding (blue) have outliers with higher CT numbers at higher energies appearing at energies above 60 keV. There also appear outliers below the box plot at energies between 100 keV and 130 keV. Thrombus (magenta) does not have any visible outliers.

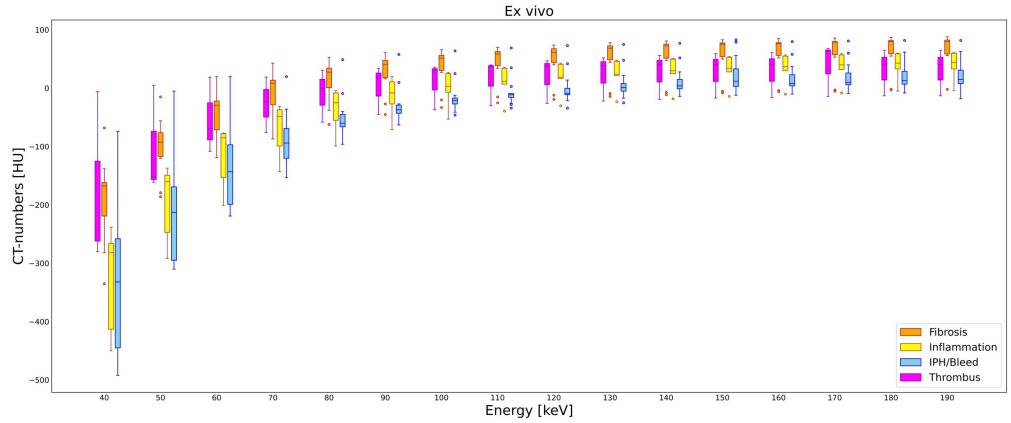

Figure 12: *Ex vivo* data with calcium is removed from the plot for the purpose of getting an overview of the soft materials. The dots represent the outliers found in each material population.

Results from the analysis of the *in vivo* scan can be seen in Figure 13. Similar results for calcium (white) as in the analysis of *ex vivo* data are seen. Note that the calcium *in vivo* measurements have lower mean CT-number when compared to *ex vivo* measurements.
Soft materials tend to have lower CT numbers at increasing energy. Soft materials reach a plateau earlier than calcium.

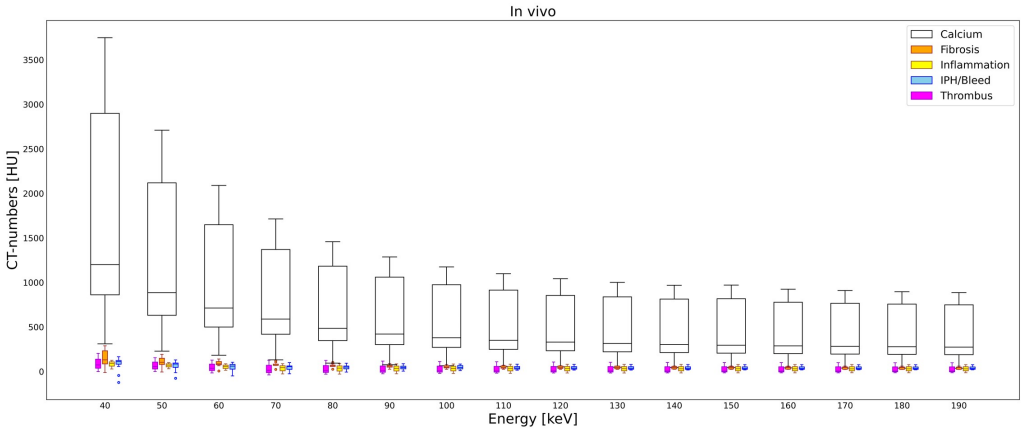

Figure 13: Box plots of the measured *in vivo* CT numbers- for the chosen ROIs for each reconstructed energy.

It can be seen in figure 14 that the outliers of fibrosis (orange) are only present at energies between 60 keV and 80 keV. IPH/ bleeding (blue) have outliers with lower CT numbers at energies between 40 keV and 50 keV. Inflammation (yellow) and thrombus (magenta) does not have any visible outliers.

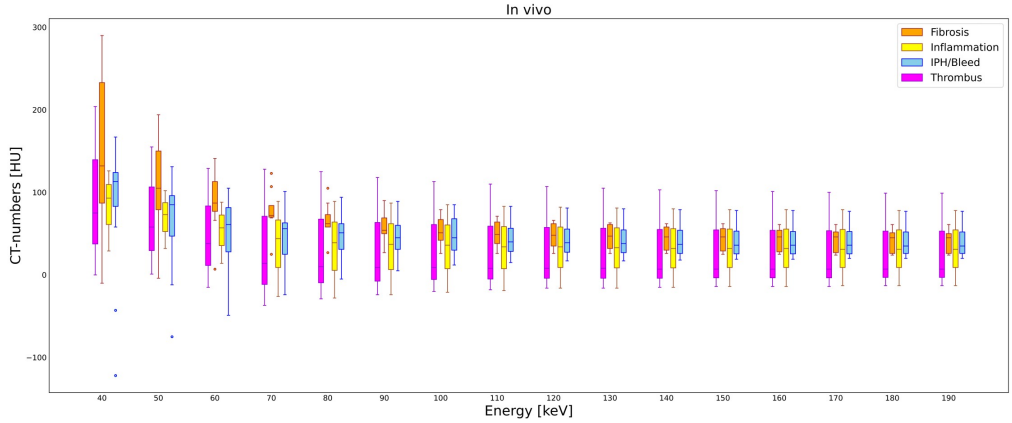

Figure 14: *In vivo* data with calcium removed from the plot for the purpose of getting an overview of the soft materials which figure 13 did not provide.

Observe figure 12 and figure 14, it can be seen that the soft materials in *ex vivo* measurements have increasing CT-numbers for higher energies while the *in vivo* measurements show the opposite. The soft tissue measurements also assume mean CT numbers close to 50 HU which is about the expected value for soft tissue.

4.1 Statistics

The results from the *ex vivo* and *in vivo* images are presented in separate tables, table 4 and 5. The tables show the mean CT number of the ROIs for each material at each reconstructed VMI (± 1 standard deviation for the values inside the ROIs).

Table 4 shows a very large standard deviation around $30-50\%$ of the mean CT-number and in the same size or bigger for thrombus.

Table 4: The table show the mean and standard deviation for *ex vivo* ROI measurements in the format mean CT number ± 1 standard deviation.

Energy [keV]/ Material CT-number [HU]	Calcium	Fibrosis	Inflammation	IPH/bleeding	Thrombus
40	3078 ± 1330	-148 ± 72	-330 ± 85	-337 ± 117	-177 ± 122
50	2137 ± 922	-71 ± 50	-197 ± 61	-210 ± 83	-103 ± 76
60	1568 ± 673	-23 ± 40	-119 ± 50	-137 ± 64	-53 ± 53
70	1261 ± 550	6 ± 37	-72 ± 43	-89 ± 45	-27 ± 39
80	981 ± 432	23 ± 35	-38 ± 35	-52 ± 36	-9 ± 37
90	828 ± 370	35 ± 33	-15 ± 32	-30 ± 31	2 ± 34
100	723 ± 328	44 ± 33	-1 ± 29	-15 ± 28	-10 ± 33
110	649 ± 298	49 ± 33	10 ± 27	-5 ± 27	15 ± 32
120	601 ± 273	55 ± 33	17 ± 26	1 ± 27	20 ± 32
130	537 ± 286	57 ± 33	23 ± 26	29 ± 26	23 ± 32
140	523 ± 248	59 ± 33	28 ± 25	13 ± 25	26 ± 32
150	499 ± 239	61 ± 33	31 ± 25	22 ± 30	27 ± 32
160	480 ± 231	63 ± 33	34 ± 24	19 ± 25	28 ± 32
170	465 ± 225	64 ± 33	36 ± 24	21 ± 25	39 ± 38
180	453 ± 221	65 ± 33	38 ± 24	22 ± 25	31 ± 32
190	445 ± 219	65 ± 33	39 ± 24	22 ± 26	31 ± 32

Table 5 shows a very large standard deviation around $30-50\%$ of the mean CT-number and in the same size or bigger for fibrosis and thrombus.

Table 5: The table show the mean and standard deviation for *in vivo* ROI measurements in the format mean CT number ± 1 standard deviation.

Energy [keV]/ Material CT-number [HU]	Calcium	Fibrosis	Inflammation	IPH/bleeding	Thrombus
40	1891 ± 1243	158 ± 92	83 ± 40	81 ± 82	93 ± 84
50	1378 ± 901	109 ± 56	69 ± 29	63 ± 57	71 ± 64
60	1076 ± 687	89 ± 38	53 ± 30	50 ± 43	51 ± 69
70	881 ± 562	78 ± 26	36 ± 47	46 ± 34	35 ± 65
80	745 ± 489	66 ± 20	33 ± 48	47 ± 28	35 ± 61
90	658 ± 438	59 ± 17	33 ± 45	46 ± 25	34 ± 57
100	598 ± 402	54 ± 16	33 ± 43	47 ± 28	34 ± 55
110	556 ± 376	51 ± 15	33 ± 42	43 ± 23	33 ± 53
120	522 ± 356	151 ± 14	33 ± 40	42 ± 21	33 ± 52
130	503 ± 344	47 ± 14	33 ± 40	42 ± 19	32 ± 51
140	486 ± 333	45 ± 14	32 ± 39	42 ± 19	32 ± 50
150	481 ± 336	44 ± 14	32 ± 38	61 ± 19	32 ± 50
160	462 ± 318	43 ± 14	32 ± 38	41 ± 18	31 ± 50
170	454 ± 313	43 ± 14	32 ± 38	41 ± 18	31 ± 50
180	447 ± 309	42 ± 14	32 ± 37	40 ± 18	31 ± 49
190	442 ± 306	42 ± 14	23 ± 37	40 ± 18	31 ± 49

The following table shows the results of the one-way ANOVA test for both *ex vivo* and *in vivo* measurements. Note that calcium is excluded from all statistical tests. The

CI = 95.0% was used for the one-way ANOVA. If the p-value is below 0.05 the one-way ANOVA show that one of the soft materials (fibrosis, inflammation, IPH/bleeding, and thrombus) is statistically significant different from the others.

Table 6: Resulting p-value of one-way ANOVA for *ex viov* and *in vivo* populations for different VMI energies.

Energy [keV]	*ex vivo*	*In vivo*
40	0.0086	0.28
50	0.0067	0.39
60	0.0034	0.29
70	0.0016	0.26
80	0.0040	0.45
90	0.0062	0.59
100	0.0091	0.70
110	0.013	0.75
120	0.019	0.81
130	0.021	0.84
140	0.027	0.85
150	0.034	0.87
160	0.034	0.89
170	0.046	0.89
180	0.040	0.89
190	0.044	0.90

It can be seen from table 6 that the one-way ANOVA showed a statistically significant difference between the different materials for all energies. The one-way ANOVA did not yield any statistical significance in the *in vivo* measurement.

The table 7 shows the result for a two-sided t-test assuming different variances for the *ex vivo* measurements. The Bonferroni correction gave the CI = 99.2%.

Table 7: p-values for two-sided t-tests when comparing two materials at a time for *ex vivo* measurements (material-pair stated in columns). p-values below 0.0083 are considered statistically significant.

Energy [keV]	Fibrosis vs. inflammation	Fibrosis vs. IPH/bleeding	Fibrosis vs. thrombus
40	0.4	0.28	0.73
50	0.93	0.0058	0.97
60	0.49	0.80	0.99
70	0.61	0.98	0.81
80	0.66	0.82	0.99
90	0.60	0.67	0.90
100	0.86	0.43	0.84
110	0.88	0.86	0.91
120	0.95	0.69	0.80
130	0.92	0.77	0.97
140	0.91	0.89	0.89
150	0.82	0.094	0.99
160	0.77	0.45	0.99
170	0.73	0.97	0.97
180	0.83	0.95	0.99
190	0.87	0.96	0.98
Energy [keV]	Inflammation vs. IPH/bleeding	Inflammation vs. thrombus	IPH/bleeding vs. thrombus
40	0.96	0.051	0.044
50	0.94	0.051	0.039
60	0.79	0.062	0.029
70	0.93	0.53	0.034
80	0.78	0.13	0.060
90	0.81	0.27	0.093
100	0.74	0.49	0.18
110	0.75	0.71	0.21
120	0.93	0.81	0.26
130	0.72	0.87	0.41
140	0.74	0.92	0.44
150	0.93	0.82	0.70
160	0.99	0.87	0.50
170	0.71	0.80	0.41
180	0.70	0.94	0.57
190	0.65	0.92	0.52

It can be seen in table 7 that the two-sided t-test assuming different variances does not yield any materials being statistically significantly different after the Bonferroni correction. However, before the correction, there would have been a significant difference between IPH/bleeding and thrombus at energies between 40-70 keV.

4.2 Conventional CT and PCCT images

The following series of figures show the conventional CT and PCCT images acquired at interesting selected slices *in vivo* and *ex vivo*. The CT-images are for a scan with 100 kV_p and the PCCT-images are res-constructed VMI at energy level 100 keV

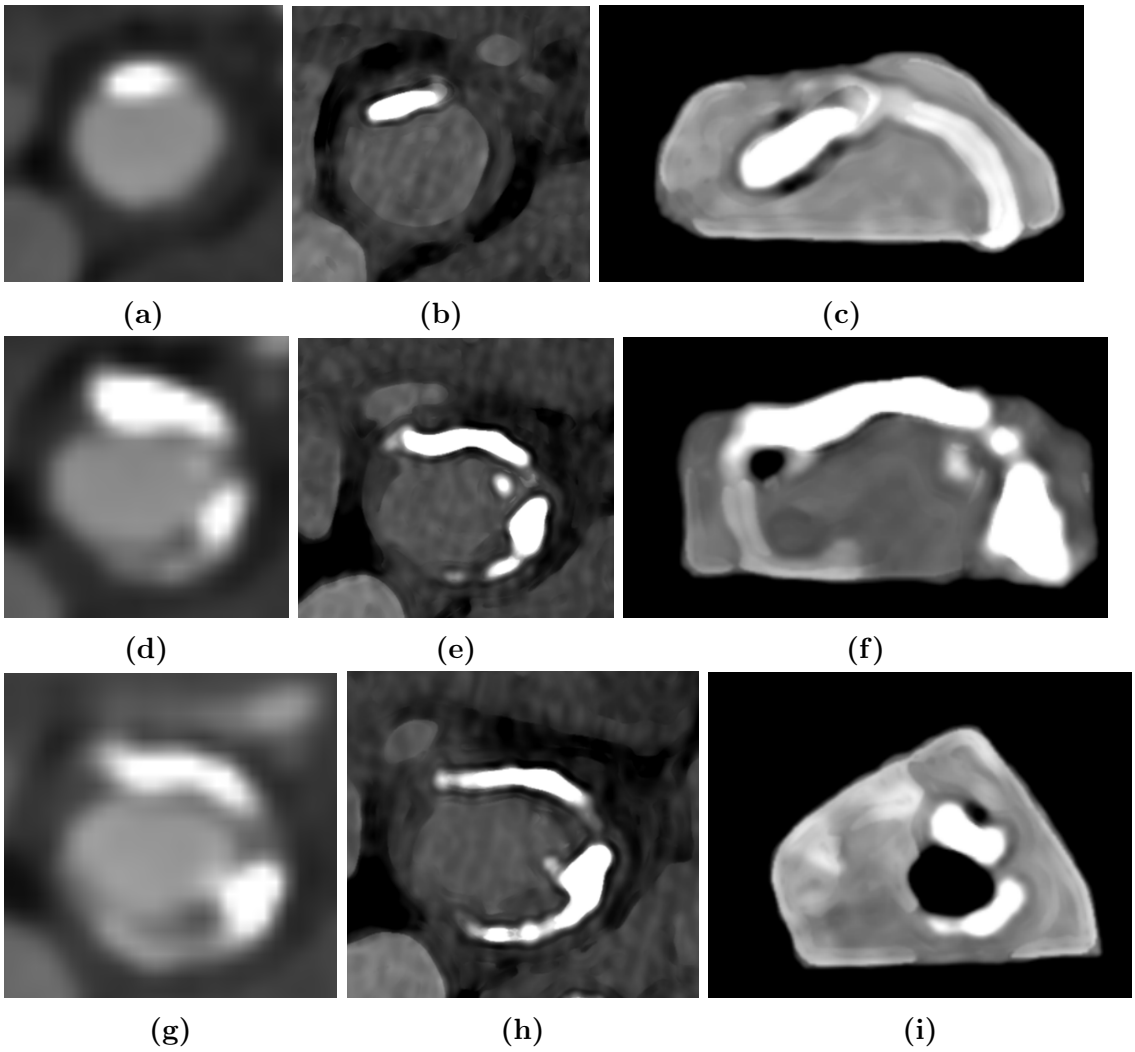

Figure 15: Each row presents a different slice (slice 1-3) of the plaque: *in vivo* with conventional CT images (left), *in vivo* with PCCT (middle) and *ex vivo* with PCCT (right). The sections are located in CCA before the bifurcation.

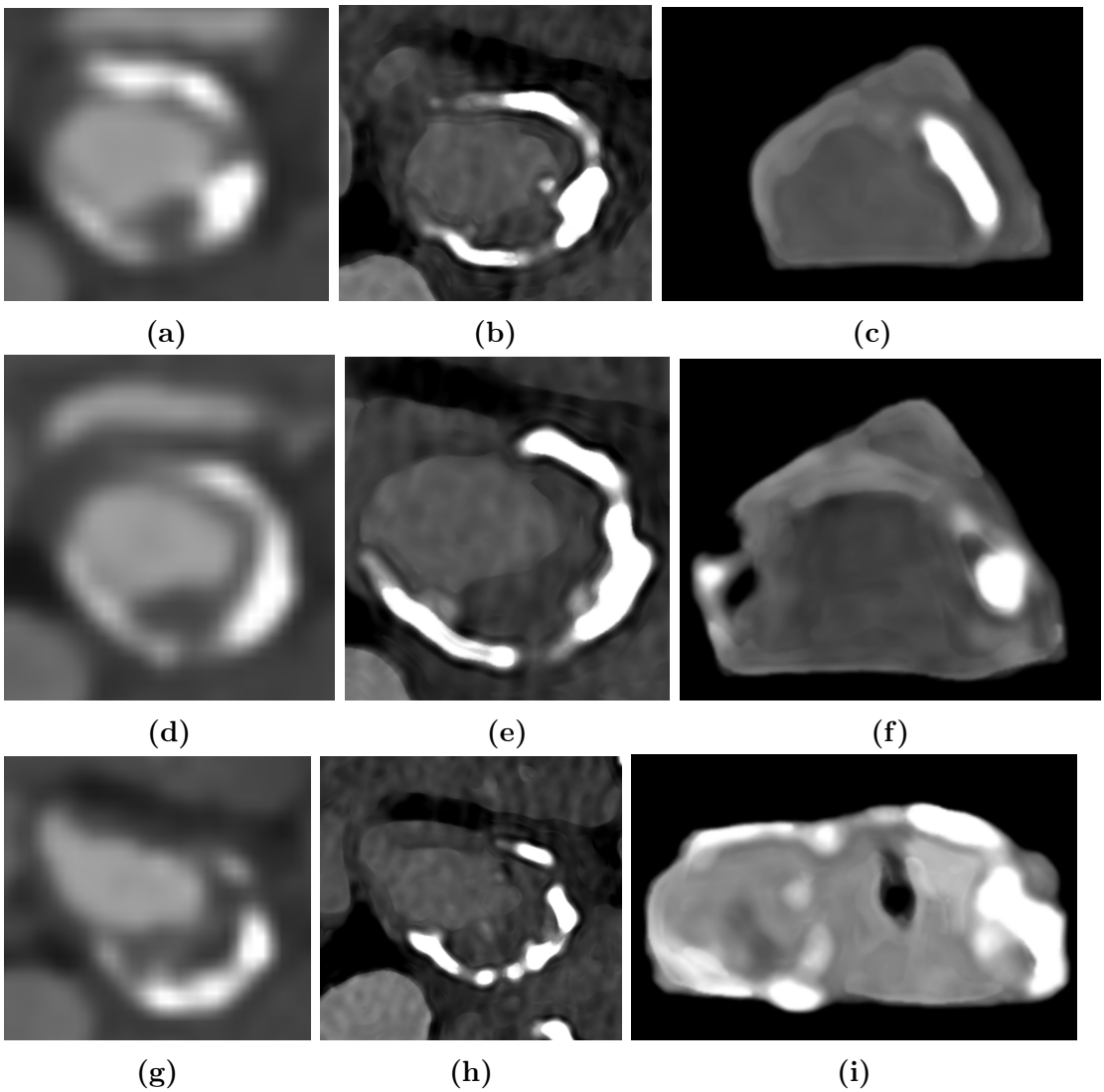

Figure 16: Each row presents a different slice (slice 4-6) of the plaque: *in vivo* with conventional CT images (left), *in vivo* with PCCT (middle) and *ex vivo* with PCCT (right). The sections are located in CCA close to the bifurcation.

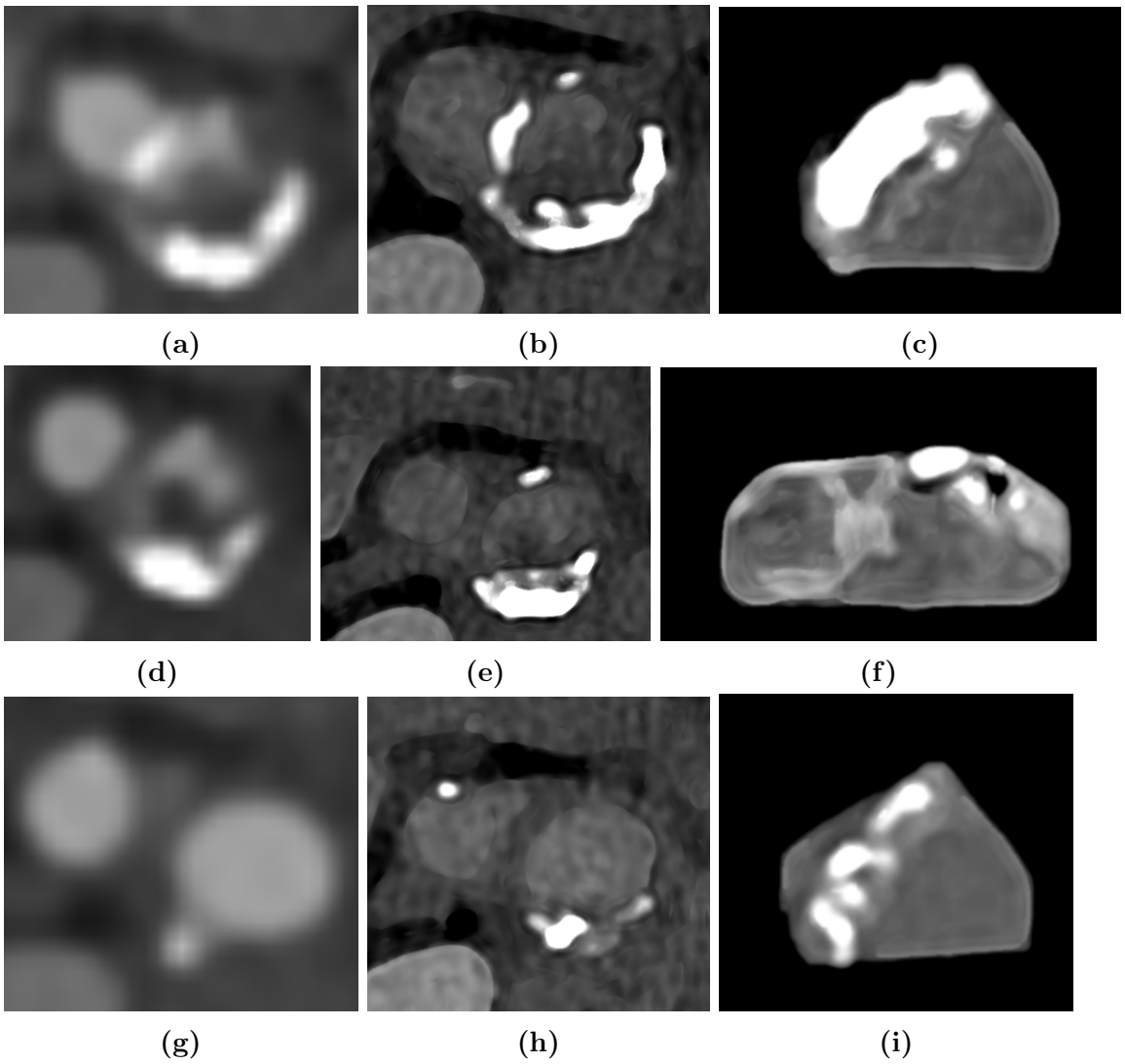

Figure 17: Each row presents a different slice (slice 7-9) of the plaque: *in vivo* with conventional CT images (left), *in vivo* with PCCT (middle) and *ex vivo* with PCCT (right). The slices are located in bifurcation making both ECA (left vessel) and ICA (right vessel) visible.

From the visual evaluation of the PCCT and the conventional CT images it was seen that calcium is prominent in all images regardless of image modality, *ex vivo* or *in vivo*. However, small pieces of calcium are almost invisible in the conventional CT images when compared to the PCCT image, see figure 17g, figure 17h and figure 17i. Thrombus is visible in both the conventional CT image and PCCT image, but it is challenging to distinguish it from the other soft tissues in the conventional image, see figure 17d, figure 17e and figure 17f. It can also be observed that the *ex vivo* images can be very different from the *in vivo*, the major reason for this is that pieces of the plaque were removed from the main mass during the surgery.

The figures below show slice 7 reconstructed for the energies 40 keV, 50 keV, 70 keV, 110 keV, 150 keV and 190 keV.

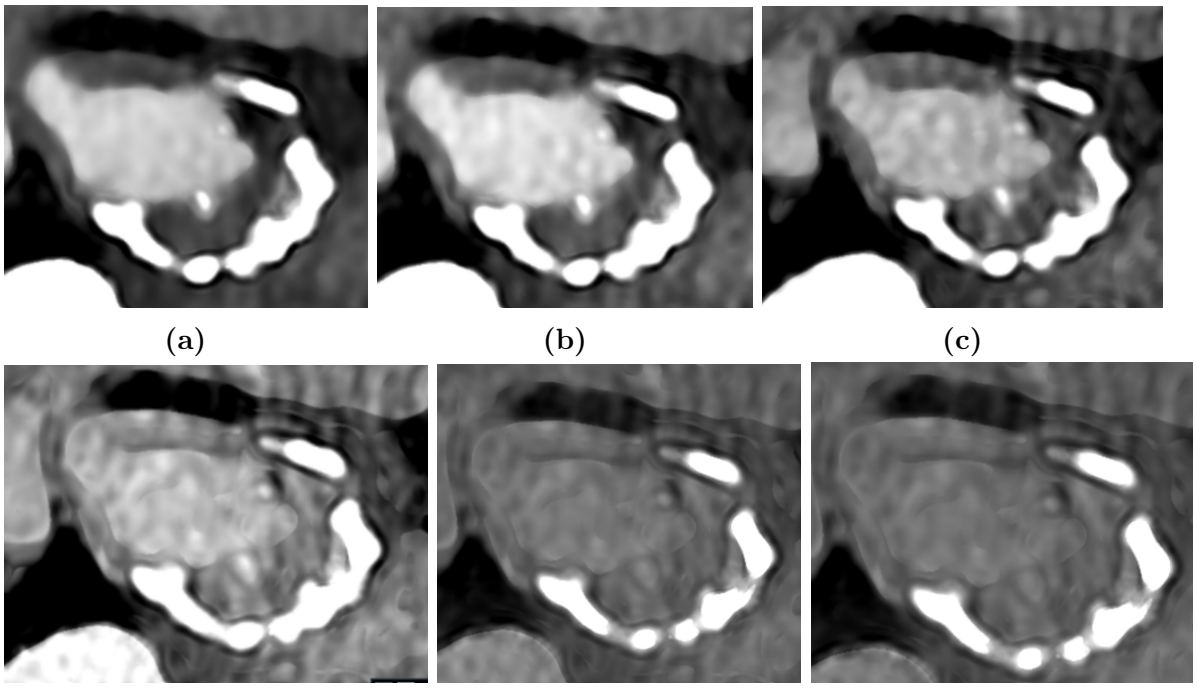

Figure 18: Different VMI reconstructions at energies 40, 50, 70, 110, 150, and 190 keV are shown in 18a-18f).

It can be seen that most calcium is enhanced at lower energies, see figure 18, while smaller calcium pieces are harder to see at higher energies. The contrast in the soft tissues is highly dependent on energy, with higher contrast at lower energies, and most contrast changes are observed between 40 and 110 keV.

4.3 Patient dose

The patient received a CTDI_{vol} (32 cm) = 13.6 mGy when scanned with the PCCT while the conventional CT gave a CTDI_{vol} (32 cm) = 11.8 mGy.

5 Discussion

5.1 Comparing histopathological images with PCCT images

A central part of this project was to compare the histopathological images with the PCCT images. It was observed that large parts of calcium were missing from *ex vivo* images when compared to corresponding *in vivo* images. The main reason for missing calcium in *ex vivo* images could be that the surgeon found it impossible to remove the plaque in one piece. The priority for the surgeon was not to remove the plaque as intact as possible but to treat the patient. If parts of the plaque were required to be removed to reach the best result for the patient then this difference in images is a result of that decision.

During the histopathology analyses, several events can lead to the sample being deformed or broken. The initial slicing of the sample can rip calcium-rich samples. Some staining methods require removing the calcium from the sample which would leave a calcium sample with only small pieces of soft tissue. It could also be seen that the plaque was more deflated in the *ex vivo* PCCT image when compared to the *in vivo* images. This can be explained by the presence of blood *in vivo* that pushes the inside of the blood vessel outwards. This means that some histopathological images were more challenging to compare with the PCCT images, increasing the uncertainty of ROI placement. The uncertainty stems from the identification of material in the histopathological image and the corresponding location in the *ex vivo* and *in vivo* images.

An unexpected observation was that it was possible to compare histopathological images with the *in vivo* images. The original workflow was to first compare the histopathological images with the *ex vivo* PCCT image and then transfer the corresponding ROIs to the *in vivo* images, due to the histopathological images being directly based on the *ex vivo* plaque. It seems that the staining of the *ex vivo* plaque retains the general structure of the plaque *in vivo*, see figure 26 in the appendix.

5.2 CT-number trends, outliers, and statistical tests

When observing the box plots of the measurement result it can be seen that the soft materials (fibrosis, inflammation. IPH/bleeding, and thrombus) in the *ex vivo* image tend to have increasing mean CT numbers at higher energies with a plateau at 120 keV. The *in vivo* image tends to have decreasing mean CT-numbers at higher energies with a plateau at 70 keV figure 12 and figure 14. This could be explained by the fact that the plaque depicted in the *ex vivo* image was dried before being encased in paraffin. This means that the sample will be completely dehydrated, creating more pronounced differences between materials. Another reason for this difference could be the surrounding material, air (*ex vivo*) compared to tissue (*in vivo*), causing different scatter conditions. The different scattering conditions could also explain why the mean CT number of the *ex vivo* measurements is higher when compared to the *in vivo* measurements.

It can be seen that calcium has the same trend of decreasing mean CT numbers with increasing energy independent of *ex vivo* and *in vivo*. However the calcium mean CT-numbers *in vivo* have a lower population mean when compared to the *ex vivo*, see figure 11 and figure 13. The unchanged trend comparing the *ex vivo* and *in vivo* can be inter-

preted as the calcium not containing water when compared to the soft materials thus being completely unaffected by the dehydration. The lower mean can be explained by the fact that the *in vivo* plaque was scanned within the patient while the *ex vivo* plaque did not have any layers of tissue around it. The surrounding tissue in the *in vivo* case creates different scatter conditions thus resulting in other CT numbers when compared to the *ex vivo* case.

The plateau behavior can be explained by the CT-number dependence of the attenuation coefficient whose Compton scatter component becomes dominant at higher energies when compared with the photoelectric effect component which is strongly dependent on X-ray energy.

The outliers that could be traced to an ROI that included two different materials were excluded due to uncertainty in correlating the CT number to a specific material. Outliers that follow the trend of their materials although having a higher (fibrosis and IPH/bleeding) or lower (fibrosis and inflammation) could be a sign of the same material but with different composition or that ROI has included a material outside of the interesting materials (fibrosis, inflammation, IPH/bleeding or thrombus).

The same consistent trend in outliers can not be found in the *in vivo* image, see 14. An interesting observation is that inflammation and thrombus, in *in vivo* measurements, do not have any visible outliers. This could be explained due to the lack of data points in these materials, see table 3. This explanation can be applied to *ex vivo* measurements where the thrombus also lacks any visible outliers.

The one-way ANOVA test yielded statistical significance for all energies when performed on the *ex vivo* measurements It can also be observed that the two-sided t-test (assuming different variances), yielded no statistical significance in differentiation materials after the Bonferroni correction. This correction decreases the power of the statistical test which means that while eliminating false positive outcomes, true positive outcomes could be excluded as well. For example, here would be statistic significant difference between IPH/bleeding and thrombus between the energies $40 - 70(keV)$. Even if this finding does not count as a true positive seeing the differences between IPH/bleeding and thrombus is very valuable because the presence of a thrombus often means that the plaque has already ruptured while IPH/bleeding is inside of a whole plaque. The statistical significance disappears at higher energies which can be explained by the definitions of the CT number and the existence of the plateau as mentioned earlier in this section. The one-way ANOVA test did not show any statistical significance for the *in vivo* measurements. It is possible that this behavior is linked to the fact that most tissues are rich in water thus making it harder to differentiate when it comes to physical properties.

5.3 Image quality and patient dose

When comparing the conventional CT image with the corresponding reconstructed VMI from the PCCT the image quality becomes obvious, see figure 15, 16 and 17. The effects of calcium blooming are major in the conventional CT images where for example adjacent calcium pieces appear to be one unit when compared to the corresponding PCCT image, see figure 22d and 17e. It can also be seen that smaller pieces of calcium

are completely invisible or appear as having a lower CT number in the conventional CT image when compared with the PCCT image, this is probably due to the partial volume effect which could give the wrong CT number, and less contrast, see figure 20d, 20c, 23d and 25c. The PCCT has smaller detector elements and thinner slice thickness which reduces the artifact. It can also be seen that the PCCT at 100 keV reduces the contrast enhancement of the lumen, facilitating visualization of calcium close to the lumen. The artery wall is more prominent in the PCCT images when compared to the conventional CT images, where it almost merges with the surrounding anatomy. The thrombus can be seen in both of the images, see figure 22d and 17e. However, the thrombus seems to be of a uniform and bigger mass in the conventional CT image when compared to the PCCT image.

The PCCT scan resulted in CTDI_{vol} (32 cm) of 13.6 mGy which is close to the conventional CT-system which resulted in CTDI_{vol} (32 cm) of 11.8 mGy. It is possible to achieve the same CTDI_{vol} as the conventional CT scan for the PCCT scan when optimizing the PCCT scan parameters. It is important to address that the PCCT scan has a superior spatial resolution when compared to conventional CT images. Furthermore, the ability to create VMI at several energies with a single scan is impossible for a conventional CT. It was observed that soft materials were best visualized at lower energies $(40 - 70(keV))$. Small calcium structures were best visualized at intermediate energies $(70 - 110(keV))$ and larger calcium structures were best viewed at higher energies $(150 - 190(keV))$. However the difference in appearance for VMI reconstructed for high energies was very small, see figure 18.

5.4 Limitations

A major limitation of the study is the fact that its results are based on only one patient. This leads to a very limited amount of measuring points (ROIs) which leads to uncertain statistics due to the very small populations. The small population can also explain the lack of statistical significance and the big influence the outliers have.

Another limitation was the placement of ROI and its size. In some cases, the ROI encircled two seemingly different materials but still had the correct location according to the histopathology. The ROIs were also very small which made the measured CT number very vulnerable to placing the ROI between materials. Due to only having access to one patient the number of measurements for each interesting material did not exceed 16 measurements at most. Furthermore, the ROI sizes were not documented during the image analysis but they were identical for each slice for all reconstructed energies. The lack of documentation will make the study harder to reproduce but it is practically unfeasible to have a set size of a ROI that depends on the size of the structure one wants to measure.

Only having one patient also limits the possible visualization of variation in plaque status (stable, vulnerable, and ruptured). The patient used in this study had a ruptured plaque. This was good in some ways because the visualization of the thrombus was possible. But it would have been interesting to see more different plaque statuses and to see if it was possible to see more rupture markers such as a fibrous cap that separates the plaque contents from the lumen and necrotic lipid core. More patients would also mean that we would have more materials (such as micro-calcium and foam cells) to

identify in the images that were excluded in this study due to the limited abundance.

There also lies a limitation in the current modality. The PCCT is still relatively new and has not yet reached its full theoretical potential. For example, it only uses two energy bins although it is possible to acquire images with four energy bins. This may further improve the spectral information and image contrast.

5.5 Other studies

Important markers for rupture and belonging to the stroke prediction model are IPH and lipid-rich necrotic core. Small calcifications at the outermost layer of the arterial wall (tunica adventitia) can also be seen as a sign of inflammation which in itself is a rupture marker. It is important to be able to view these markers due to the fact that the degree of stenosis not being a strong marker for plaque rupture [31]. Calcification close to the luminal border can be difficult to discriminant from the lumen containing contrast medium in conventional CT images due to calcium blooming artifact. Furthermore, all soft material rupture markers have relatively similar CT numbers which make it hard to discriminate at clinical CT systems [8]. Calcium blooming artifacts also causes difficulties to define the calcium size and it can also obscure the content of the plaque, which can affect the evaluation of the degree of stenosis [25, 30, 32].

6 Conclusion

It is clear that this study's greatest limitation is the small data set obtained from only one patient. It is thus not possible to draw any conclusions from the statistical analyses. But the general trend of the CT numbers of the interesting soft materials (fibrosis, inflammation, IPH/bleeding, and thrombus) indicates that there is a detectable difference in physical and attenuating properties between them. It can also be assumed that the dehydration of the surgically removed plaque will affect the trend of the CT numbers of the soft materials. An important finding was also that it was possible to correlate the histopathology images directly with the *in vivo* images.

The visual observation of the PCCT images provide much more details and a variety of contrast thanks to the possibility of reconstructing VMIs when compared to the conventional CT image. The PCCT images do not seem to be as affected by the calcium blooming artifact. The artifact is a major reason for the degradation of the image. It can make the location of calcium near the luminal border hard and it can also obscure the overall plaque contents. Furthermore, the PCCT small slice thickness decreases the amount of calcium blooming effects which in earlier studies have been reported to hide important structures markers to identify vulnerable plaque. Even if the statistics remain inconclusive the visual improvement when comparing PCCT images with conventional CT images will have great value in the evaluations already existing in the clinic, that is better measurements of the degree of stenosis due to less calcium blooming.

6.1 Future prospects

If more patients are available with different plaque status then more markers for rupture could be measured, such as fibrous cap and necrotic lipid core. More patients will also mean higher statistical power and more reliable results. If the PCCT images were acquired with more than two energy bins material decomposition would be possible. This type of reconstruction could make more information about similar materials available to the viewer thus differentiation of the materials could become better. Continuing this research could lead to new and improved ways to evaluate carotid atherosclerotic stenosis, which may improve the treatment and prognosis for the patients.

7 Acknowledgements

Gratitude to all how made the completion of my master thesis possible.

Marie-Louise Aurumskjöld, thank you for the valuable discussions and incredible support during this semester.

Veronica Fransson, thank you for always being available to give awesome feedback regardless of the hour of the day.

Kristina Ydström, thank you for the important advises only an very experienced person could give.

Isabel Gonçalves, **Annelie Shami** , **Chrysostomi Gialeli**, **Lena Sundius** and **Ana Persson** thank you for the incredible expertise in medicine, histopathology and patient logistics.

Thank you to the **Patient** for making a difference by participating in this study.

References

[1] Cheng SF, van Velzen TJ, Gregson J, Richards T, Jäger HR, Simister R, et al. The 2nd European Carotid Surgery Trial (ECST-2): rationale and protocol for a randomised clinical trial comparing immediate revascularisation versus optimised medical therapy alone in patients with symptomatic and asymptomatic carotid stenosis at low to intermediate risk of stroke [Journal Article]. Trials. 2022;23(1):606. Doi: 10.1186/s13063-022-06429-z.

[2] Svenska MeSH [Internet]; 2023. Stocholm: Karolinska Institutet. Universitetsbiblioteket; 1998-. Ischemic Attack, Transient [cited 30-03-2023]. Available from: `https://mesh.kib.ki.se/term/D002546/ischemic-attack-transient`.

[3] Svenska MeSH [Internet]; 2023. Stocholm: Karolinska Institutet. Universitetsbiblioteket; 1998-. Ischemic Stroke [cited 30-03-2023]. Available from: `https://mesh.kib.ki.se/term/D000083242/ischemic-stroke`.

[4] Svenska MeSH [Internet]; 2023. Stocholm: Karolinska Institutet. Universitetsbiblioteket; 1998-. Embolism and Thrombosis [cited 31-03-2023]. Available from: `https://mesh.kib.ki.se/term/D016769/embolism-and-thrombosis`.

[5] Medibas [Internet]; 2023. Stocholm: 1997-. Karotisstenos [cited 25-02-2023]. Available from: `https://medibas.se/handboken/kliniska-kapitel/hjarta-karl/tillstand-och-sjukdomar/karlsjukdom/karotisstenos`.

[6] Stary HC, Chandler AB, Dinsmore RE, Fuster V, Glagov S, Insull J W, et al. A definition of advanced types of atherosclerotic lesions and a histological classification of atherosclerosis. A report from the Committee on Vascular Lesions of the Council on Arteriosclerosis, American Heart Association [Journal Article]. Circulation. 1995;92(5):1355-74. Doi: 10.1161/01.cir.92.5.1355.

[7] Nighoghossian N, Derex L, Douek P. The vulnerable carotid artery plaque: current imaging methods and new perspectives [Journal Article]. Stroke. 2005;36(12):2764-72. Doi: 10.1161/01.Str.0000190895.51934.43.

[8] Baradaran H, Gupta A. Carotid Vessel Wall Imaging on CTA [Journal Article]. AJNR Am J Neuroradiol. 2020;41(3):380-6. Doi: 10.3174/ajnr.A6403.

[9] Shi X, Gao J, Lv Q, Cai H, Wang F, Ye R, et al. Calcification in Atherosclerotic Plaque Vulnerability: Friend or Foe? [Journal Article]. Front Physiol. 2020;11:56. Doi: 10.3389/fphys.2020.00056. eCollection 2020.

[10] Varrassi M, Sferra R, Gravina GL, Pompili S, Fidanza RC, Ventura M, et al. Carotid artery plaque characterization with a wide-detector computed tomography using a dedicated post-processing 3D analysis: comparison with histology [Journal Article]. Radiol Med. 2019;124(9):795-803. Doi: 10.1007/s11547-019-01026-8.

[11] Benson JC, Nardi V, Bois MC, Saba L, Brinjikji W, Savastano L, et al. Correlation between computed tomography angiography and histology of carotid artery atherosclerosis: Can semi-automated imaging software predict a plaque's composition? [Journal Article]. Interv Neuroradiol. 2022;28(3):332-7. Doi: 10.1177/15910199211031093.

[12] Flohr T, Petersilka M, Henning A, Ulzheimer S, Ferda J, Schmidt B. Photon-counting CT review [Journal Article]. Physica Medica. 2020;79:126-36. Doi: 10.1016/j.ejmp.2020.10.030.

[13] Leng S, Bruesewitz M, Tao S, Rajendran K, Halaweish AF, Campeau NG, et al. Photon-counting Detector CT: System Design and Clinical Applications of an Emerging Technology [Journal Article]. Radiographics. 2019;39(3):729-43. Doi: 10.1148/rg.2019180115.

[14] Greffier J, Villani N, Defez D, Dabli D, Si-Mohamed S. Spectral CT imaging: Technical principles of dual-energy CT and multi-energy photon-counting CT [Journal Article]. Diagnostic and Interventional Imaging. 2022. Doi: 10.1016/j.diii.2022.11.003.

[15] Taguchi K. Spectral, photon counting computed tomography. technology and applications. First edition. ed. Devices, circuits, & systems. CRC Press, Taylor & Francis Group; 2020.

[16] Aurumskjöld ML. Optimisation of image quality and radiation dose in computed tomography using iterative image reconstruction [Doctoral Thesis (compilation)]; 2017. ISSN: 1652-8220 Lund University, Faculty of Medicine Doctoral Dissertation Series 2017:116.

[17] McCollough CH, Boedeker K, Cody D, Duan X, Flohr T, Halliburton SS, et al. Principles and applications of multienergy CT: Report of AAPM Task Group 291 [Journal Article]. Medical Physics. 2020;47(7):e881-912. Doi: 10.1002/mp.14157.

[18] Schofield R, King L, Tayal U, Castellano I, Stirrup J, Pontana F, et al. Image reconstruction: Part 1 – understanding filtered back projection, noise and image acquisition [Journal Article]. Journal of Cardiovascular Computed Tomography. 2020;14(3):219-25. Doi: 10.1016/j.jcct.2019.04.008.

[19] Willemink M, Persson M, Pourmorteza A, Pelc N, Fleischmann D. Photon-counting CT: Technical Principles and Clinical Prospects [Journal Article]. Radiology. 2018;289:172656. Doi: 10.1148/radiol.2018172656.

[20] Shanblatt E, O'Doherty J, Petersilka M, Wolber P, Fung G, Ramirez-Giraldo JC. NAEOTOM Alpha with Quantum Technology: How photon-counting CT works and the benefits it provides; 2022.

[21] McCollough CH, Leng S, Yu L, Fletcher JG. Dual- and Multi-Energy CT: Principles, Technical Approaches, and Clinical Applications [Journal Article]. Radiology. 2015;276(3):637-53. Doi: 10.1148/radiol.2015142631.

[22] Sartoretti T, Racine D, Mergen V, Jungblut L, Monnin P, Flohr TG, et al. Quantum Iterative Reconstruction for Low-Dose Ultra-High-Resolution Photon-Counting Detector CT of the Lung [Journal Article]. Diagnostics (Basel). 2022;12(2). Doi: 10.3390/diagnostics12020522.

[23] Stiller W. Basics of iterative reconstruction methods in computed tomography: A vendor-independent overview [Journal Article]. European Journal of Radiology. 2018;109:147-54. Doi: 10.1016/j.ejrad.2018.10.025.

[24] Faycal K. Chapter 4. In: Faycal K, editor. Mathematics and Physics of Computed Tomography (CT): Demonstrations and Practical Examples. Rijeka: IntechOpen; 2013. p. 81-106. Doi: 10.5772/52351.

[25] Pack JD, Xu M, Wang G, Baskaran L, Min J, De Man B. Cardiac CT blooming artifacts: clinical significance, root causes and potential solutions [Journal Article]. Visual Computing for Industry, Biomedicine, and Art. 2022;5(1):29. Doi: 10.1186/s42492-022-00125-0.

[26] Britannica [Internet]; 2023. Encyclopædia Britannica. 1768-. Artery [cited 25-02-2023]. Available from: `https://www.britannica.com/science/artery`.

[27] Svenska MeSH [Internet]; 2023. Stocholm: Karolinska Institutet. Universitetsbiblioteket; 1998-. Carotid Artery Diseases [cited 17-02-2023]. Available from: `https://mesh.kib.ki.se/term/D002340/carotid-artery-diseases`.

[28] Svenska MeSH [Internet]; 2023. Stocholm: Karolinska Institutet. Universitetsbiblioteket; 1998-. Atherosclerosis [cited 17-02-2023]. Available from: `https://mesh.kib.ki.se/term/D001161/arteriosclerosis`.

[29] Rothwell PM, Gibson RJ, Slattery J, Sellar RJ, Warlow CP. Equivalence of measurements of carotid stenosis. A comparison of three methods on 1001 angiograms. European Carotid Surgery Trialists' Collaborative Group [Journal Article]. Stroke. 1994;25(12):2435-9. Doi: 10.1161/01.str.25.12.2435.

[30] Karlöf E, Buckler A, Liljeqvist ML, Lengquist M, Kronqvist M, Toonsi MA, et al. Carotid Plaque Phenotyping by Correlating Plaque Morphology from Computed Tomography Angiography with Transcriptional Profiling [Journal Article]. Eur J Vasc Endovasc Surg. 2021;62(5):716-26. Doi: 10.1016/j.ejvs.2021.07.011.

[31] Baradaran H, Eisenmenger LB, Hinckley PJ, de Havenon AH, Stoddard GJ, Treiman LS, et al. Optimal Carotid Plaque Features on Computed Tomography Angiography Associated With Ischemic Stroke [Journal Article]. Journal of the American Heart Association. 2021;10(5):e019462. Doi: 10.1161/JAHA.120.019462.

[32] Diab HMH, Rasmussen LM, Duvnjak S, Diederichsen A, Jensen PS, Lindholt JS. Computed tomography scan based prediction of the vulnerable carotid plaque [Journal Article]. BMC Med Imaging. 2017;17(1):61. Doi: 10.1186/s12880-017-0233-5.

Appendix

Chosen ROI in PCCT images

The following section contains the image slices used when gathering the data to analyze. The ROI colors define which material the ROI contains. The colors of the ROIs are designated to one material as follows: white- calcium, orange - fibrosis, yellow - inflammation, blue - IPH/bleeding, and magenta - thrombus.

1444A CCA at bifurcation

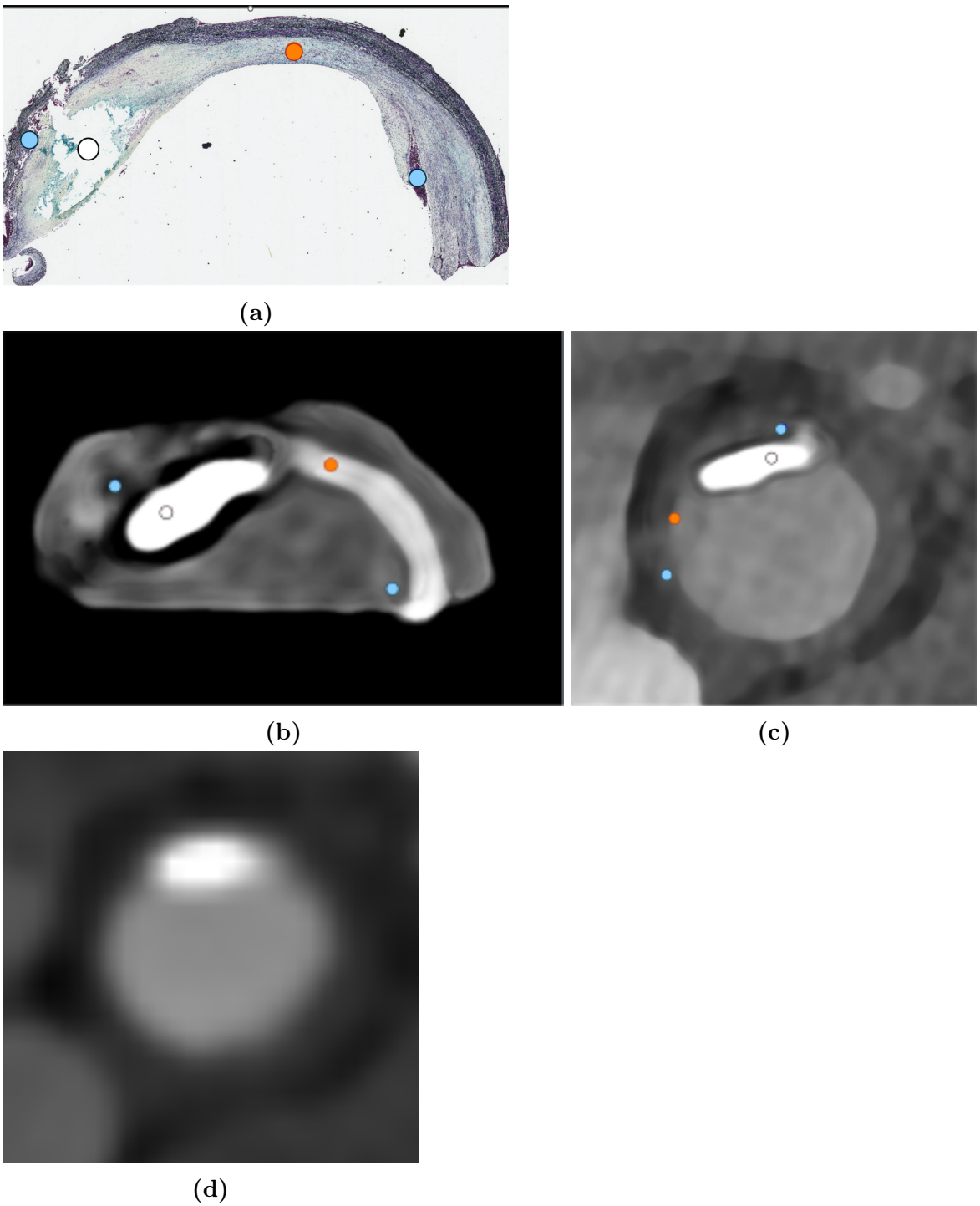

(a) **(b)** **(c)** **(d)**

Figure 19: Figure 19a show the histology result of Image 190/485 *ex vivo* 4.0 mm from label. Figure 19b and figure 19c show the 60 keV VMI of *ex vivo* and *in vivo* respectively, where the *in vivo* image number is 97/161. Figure 19d shows the corresponding location acquired by a conventional CT, the image number is 485/846. Form 1444A

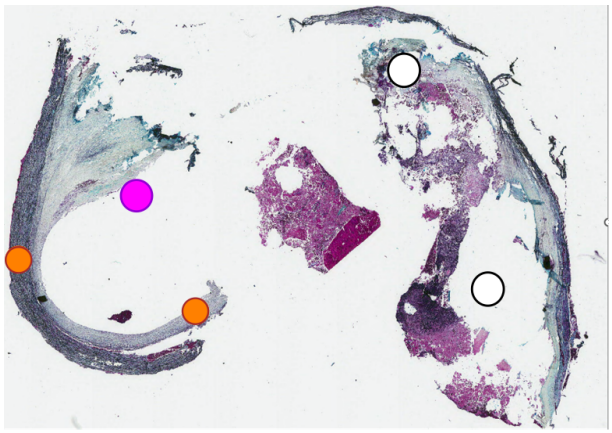

(a)

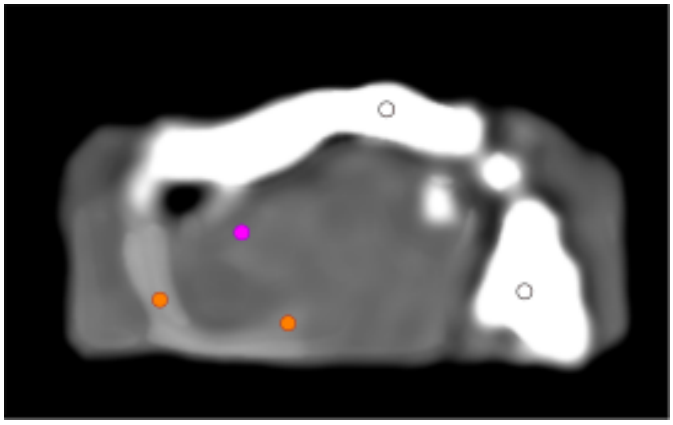

(b)

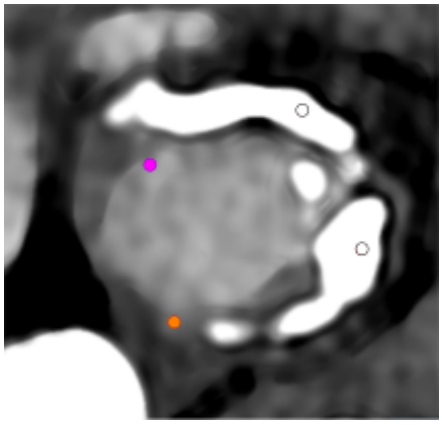

(c)

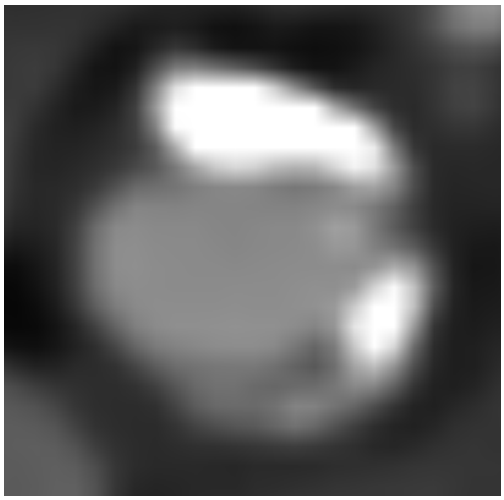

(d)

Figure 20: Figure 20a show the histology result of Image 182/485 *ex vivo* 7.2 mm from label. Figure 20b and figure 20c show the 60 keV VMI of *ex vivo* and *in vivo* respectively, where the *in vivo* image number is 99/161. Figure 20d show the corresponding location acquired by a conventional CT, the image number is 481/846. from 1444A

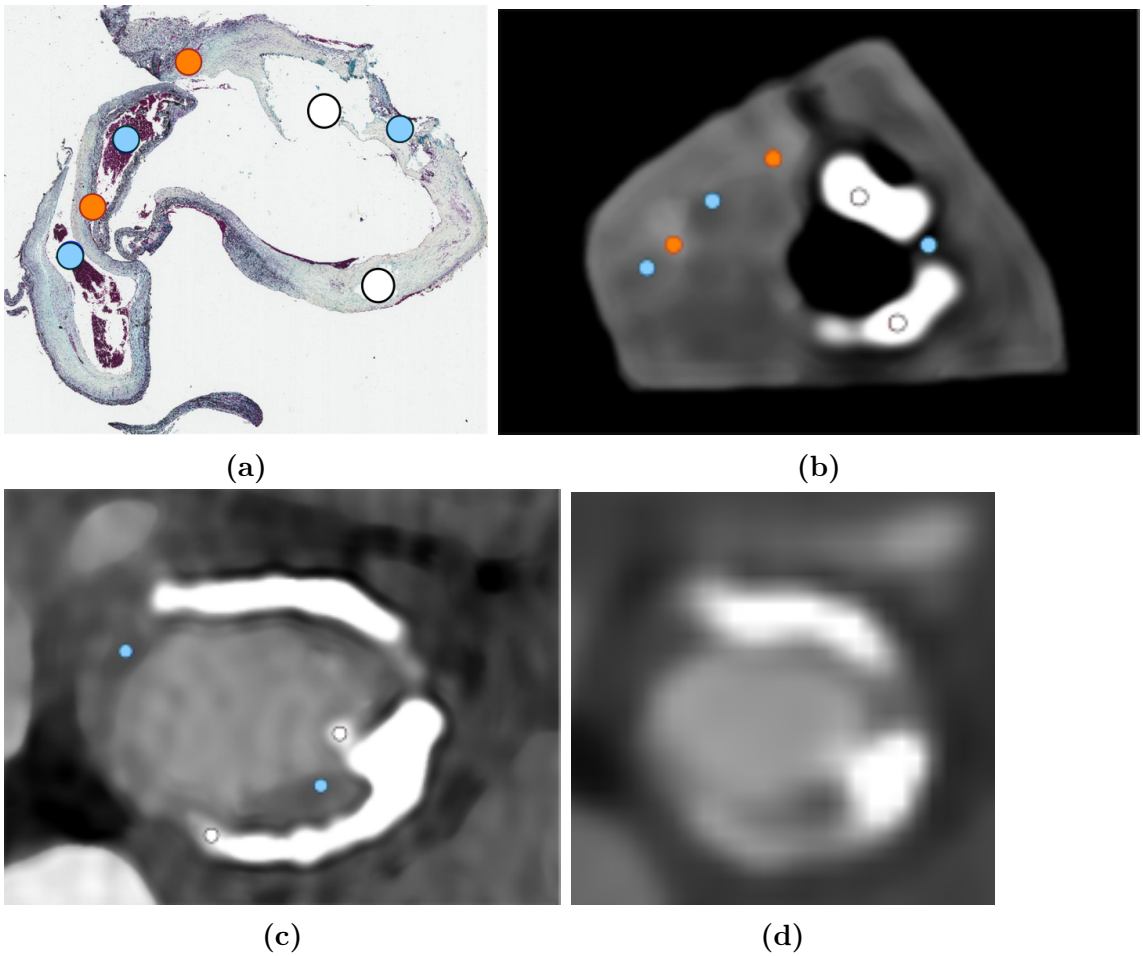

(a) **(b)**

(c) **(d)**

Figure 21: Figure 21a show the histology result of Image 438/485 *ex vivo* 5.6 mm from label. Figure 21b and figure 21c show the 60 keV VMI of *ex vivo* and *in vivo* respectively, where the *in vivo* image number is 97/161. Figure 21d shows the corresponding location acquired by a conventional CT, the image number is 479/846. From 1444B

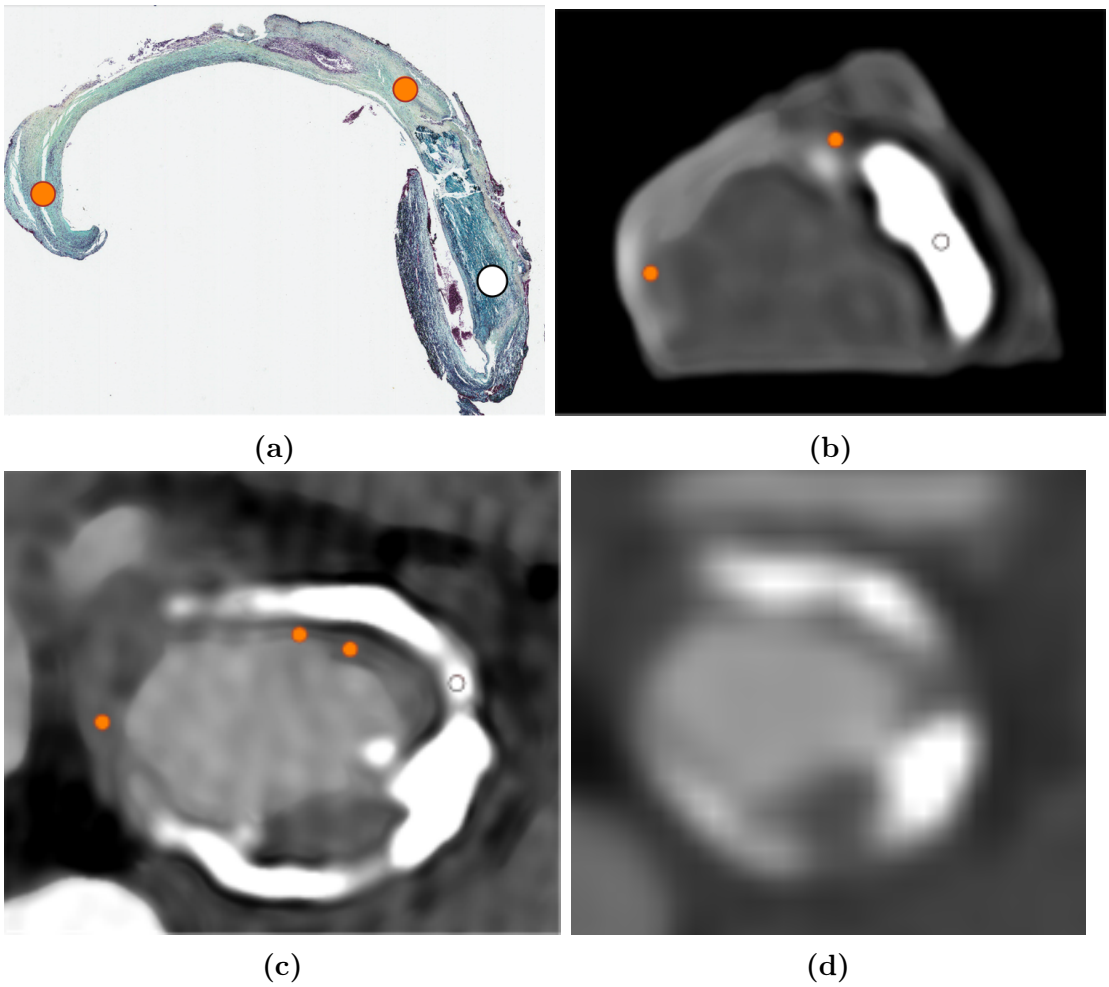

(a) **(b)**

(c) **(d)**

Figure 22: Figure 22a show the histology result of Image 438/485 *ex vivo* 8.0 mm from label. Figure 22b and figure 22c show the 60 keV VMI of *ex vivo* and *in vivo* respectively, where the *in vivo* image number is 96/161. Figure 22d shows the corresponding location acquired by a conventional CT, the image number is 478/846. From 1444B

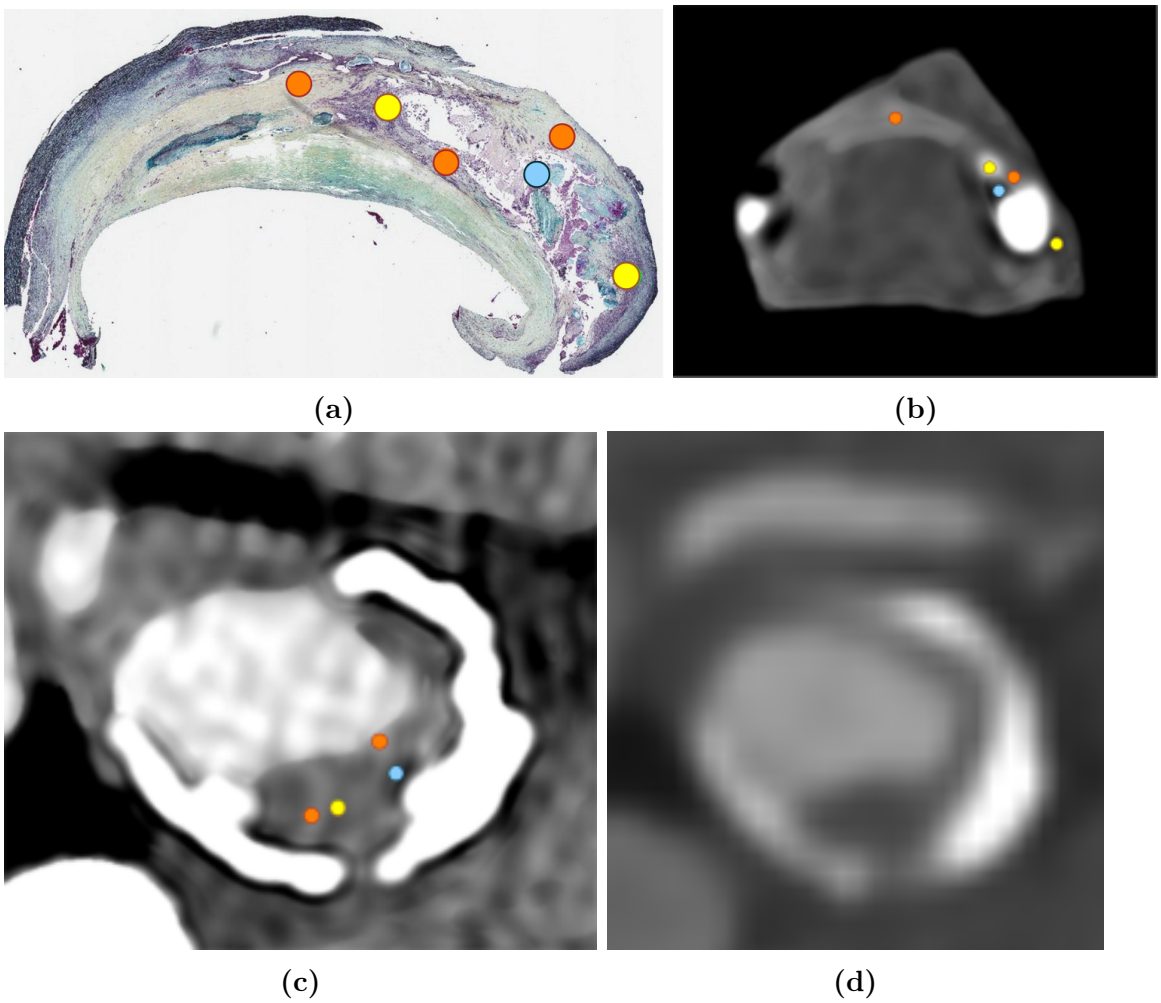

Figure 23: Figure 23a shows the histology result of Image 438/485 *ex vivo* 10.0 mm from the label. Figure 23b and figure 23c show the 60 keV VMI of *ex vivo* and *in vivo* respectively, where the *in vivo* image number is 93/161. Figure 23d shows the corresponding location acquired by a conventional CT, the image number is 427/846. From 1444 B

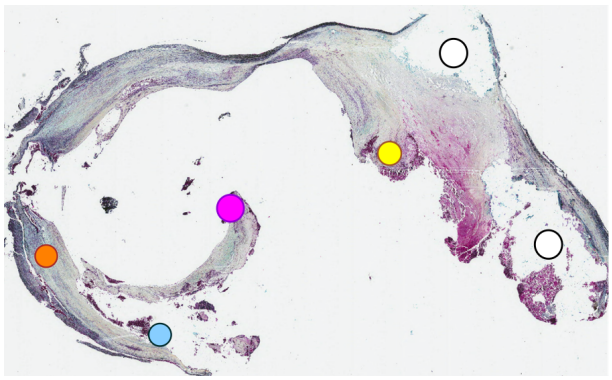

(a)

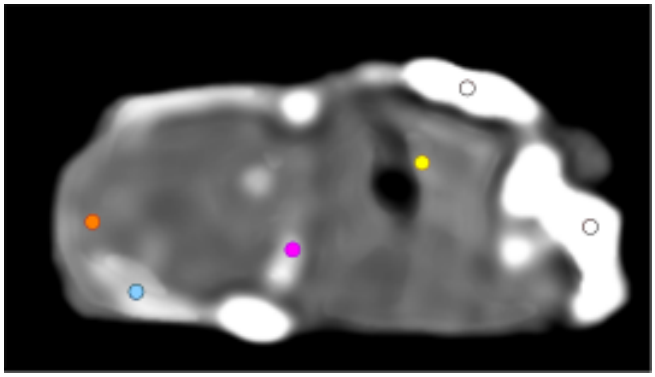

(b)

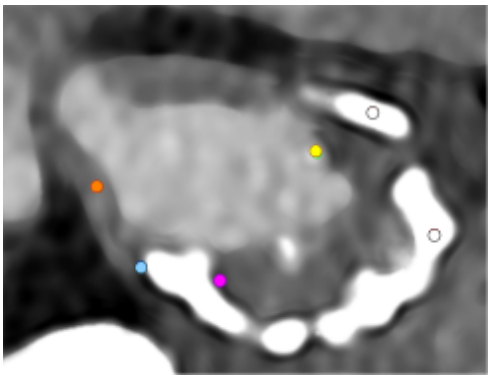

(c)

(d)

Figure 24: Figure 24a show the histology result of Image 174/485 *ex vivo* 10.4 mm from label. Figure 24b and figure 24c show the 60 keV VMI of *ex vivo* and *in vivo* respectively, where the *in vivo* image number is 91/161. Figure 24d shows the corresponding location acquired by a conventional CT, the image number is 471/846. From 1444A

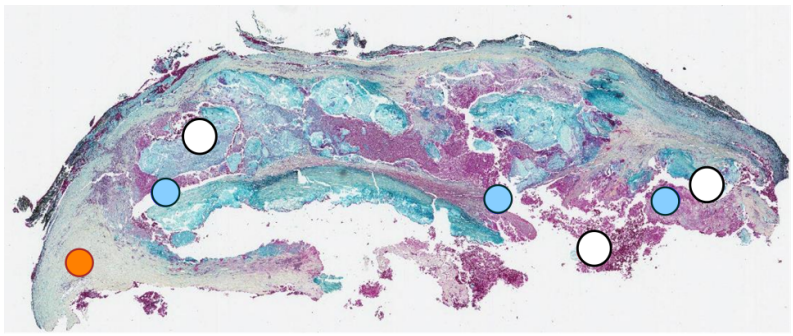

(a)

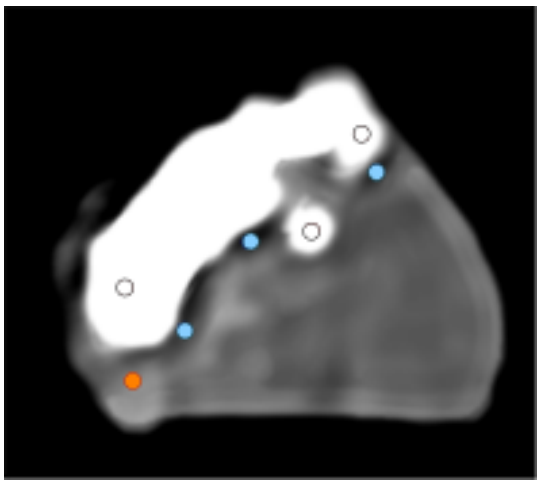

(b)

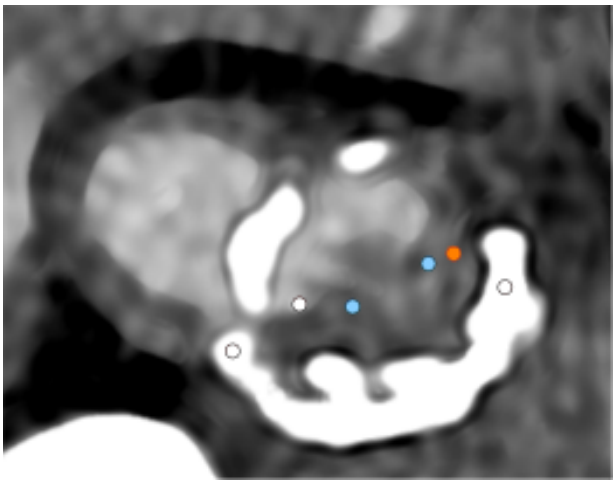

(c)

(d)

Figure 25: Figure 25a show the histology result of Image 409/485 *ex vivo* 17. 0 mm from the label. Figure 25b and figure 25c show the 60 keV VMI of *ex vivo* and *in vivo* respectively, where the *in vivo* image number is 86/161. Figure 25d shows the corresponding location acquired by a conventional CT, the image number is 469/846. From 1444B

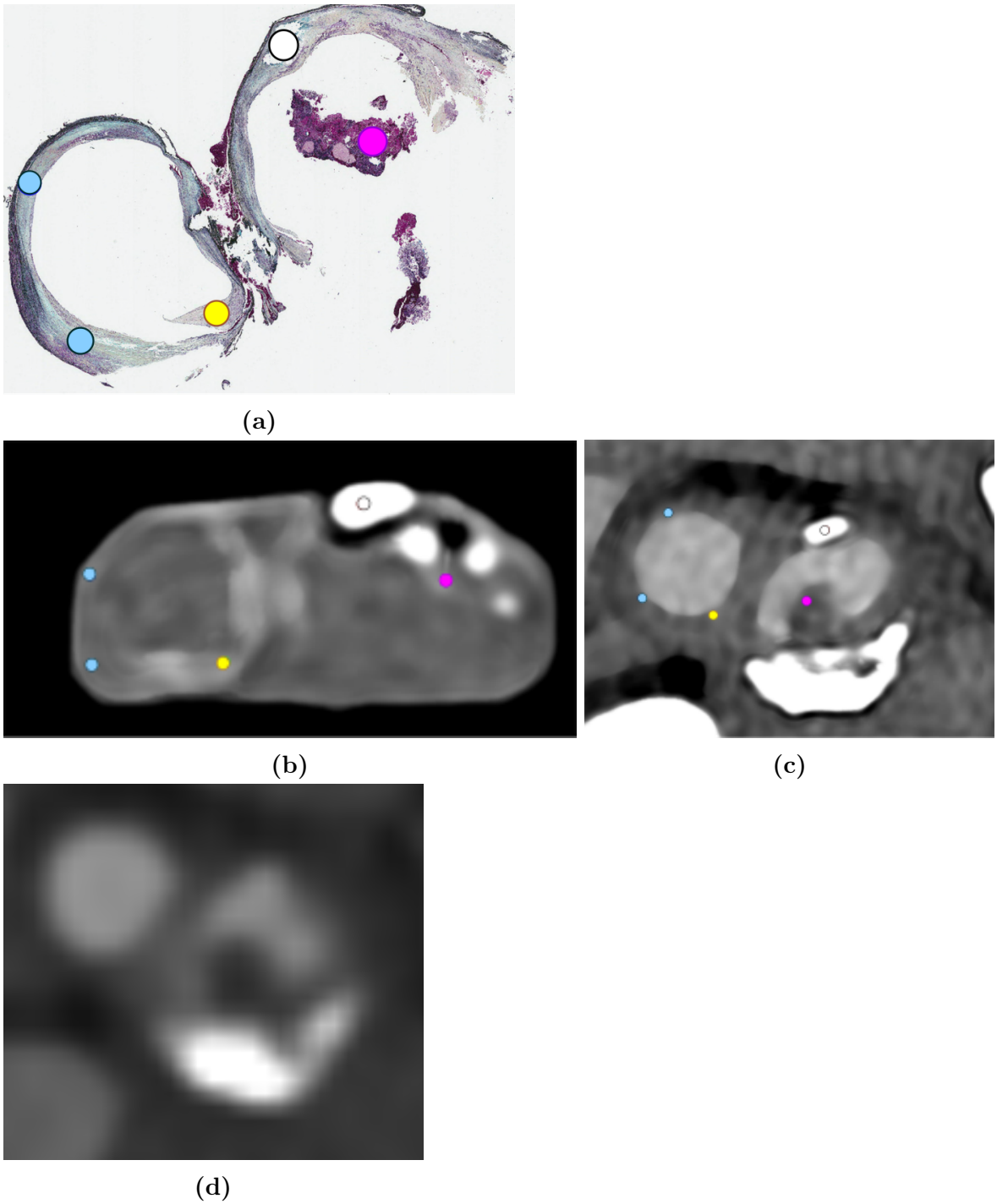

(a)

(b)

(c)

(d)

Figure 26: Figure 26a show the histology result of Image 165/485 *ex vivo* 14.0 mm from label. Figure 26b and figure 26c show the 60 keV VMI of *ex vivo* and *in vivo* respectively, where the *in vivo* image number is 82/161. Figure 26d shows the corresponding location acquired by a conventional CT, the image number is 467/846. From 1444A

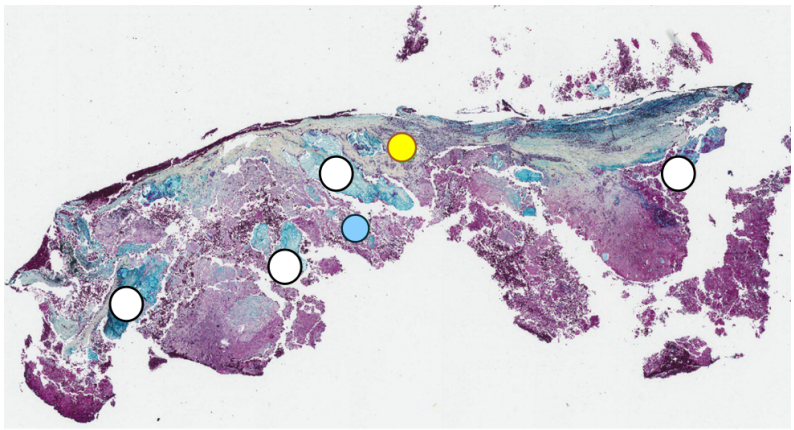

(a)

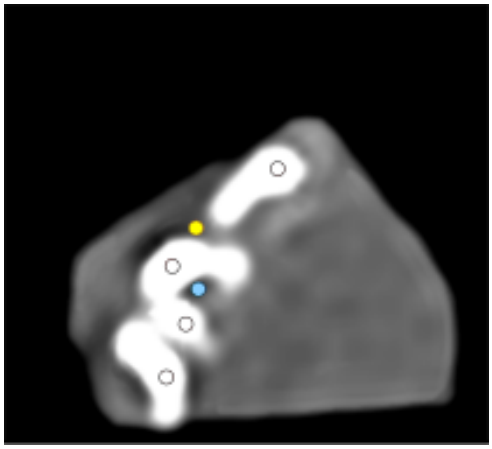

(b)

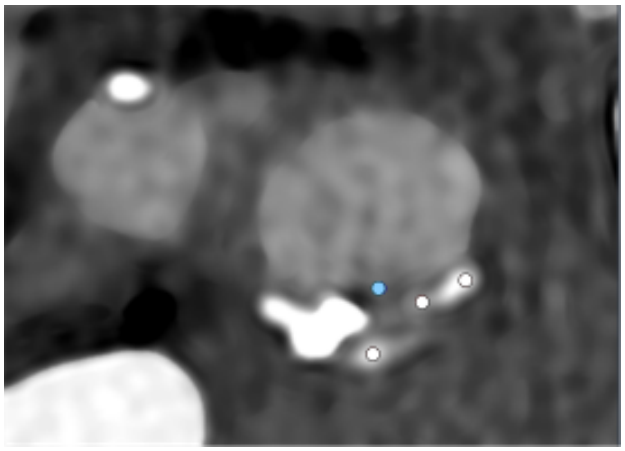

(c)

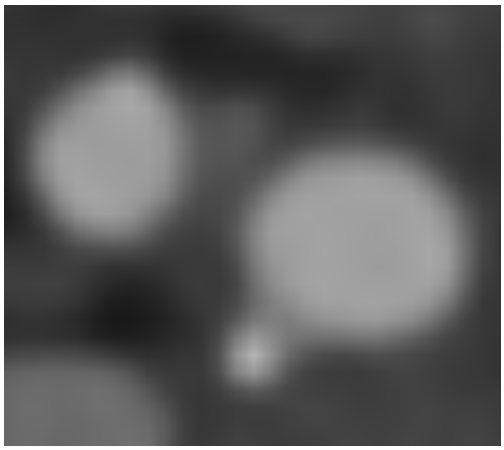

(d)

Figure 27: Figure 27a show the histology result of Image 400/485 *ex vivo* 20.8 mm from label. Figure 27b and figure 27c show the 60 keV VMI of *ex vivo* and *in vivo* respectively, where the *in vivo* image number is 76/161. Figure 27d shows the corresponding location acquired by a conventional CT, the image number is 459/846. from 1444B